

Doctoral Thesis in Theoretical Physics

The supernova cosmology cookbook: Bayesian numerical recipes

Natallia V. Karpenka

Oskar Klein Centre for
Cosmoparticle Physics
and Cosmology,
Particle Astrophysics
and String Theory

Department of Physics
Stockholm University
SE-106 91 Stockholm

Stockholm, Sweden 2014



**Stockholm
University**

Cover image: Cosmology princess cake. See Appendix A. Credit: Dr. Oscar Larsson

ISBN 978-91-7447-953-9 (pp. i–xxii, 1–98)
pp. i–xxii, 1–98 © Natallia V. Karpenka, 2014

Printed by Universitetsservice US-AB, Stockholm, Sweden, 2014.

Figures 1.2, 1.3, 1.5, 2.1, 2.2, 2.3, 3.1, 3.3 and 4.4 used with permission.

Typeset in pdf \LaTeX

Посвящается
дедушке Михаилу Тимофеевичу Назарчуку
и бабушке Эмме Владимировне Карпенко.

Abstract

Theoretical and observational cosmology have enjoyed a number of significant successes over the last two decades. Cosmic microwave background measurements from the Wilkinson Microwave Anisotropy Probe and Planck, together with large-scale structure and supernova (SN) searches, have put very tight constraints on cosmological parameters. Type Ia supernovae (SNIa) played a central role in the discovery of the accelerated expansion of the Universe, recognised by the Nobel Prize in Physics in 2011.

The last decade has seen an enormous increase in the amount of high quality SN observations, with SN catalogues now containing hundreds of objects. This number is expected to increase to thousands in the next few years, as data from next-generation missions, such as the Dark Energy Survey and Large Synoptic Survey Telescope become available. In order to exploit the vast amount of forthcoming high quality data, it is extremely important to develop robust and efficient statistical analysis methods to answer cosmological questions, most notably determining the nature of dark energy.

To address these problems my work is based on nested-sampling approaches to parameter estimation and model selection and neural networks for machine-learning. Using advanced Bayesian techniques, I constrain the properties of dark-matter haloes along the SN lines-of-sight via their weak gravitational lensing effects, develop methods for classifying SNe photometrically from their lightcurves, and present results on more general issues associated with constraining cosmological parameters and testing the consistency of different SN compilations.

Svensk sammanfattning

Teoretisk och observationell kosmologi har åtnjutit många viktiga framgångar de senaste årtiondena. Mätningar av den kosmiska mikrovågsbakgrunden från Wilkinson Microwave Anisotropy Probe and Planck, tillsammans med undersökningar av Universums storskaliga struktur och supernovor, har satt stränga begränsningar på de kosmologiska parametrarna. Supernovor av Typ Ia spelade en central roll i upptäckten av Universums accelererade expansion, en upptäckt som belönades med Nobelpriset 2011.

Det senaste årtiondet har fört med sig en enorm ökning av mängden högkvalitativa observationer av supernovor, och kataloger innehåller nu hundratals objekt. Detta antal förväntas öka till tusentals inom de närmsta åren i och med att data från nästa generations observationer som Dark Energy Survey och Large Synoptic Survey Telescope blir tillgängliga. För att kunna utnyttja den stora mängden kommande data är det extremt viktigt att utveckla robusta och effektiva tekniker för statistisk analys för att kunna svara på de kosmologiska frågeställningarna, framför allt gällande den mörka energins beskaffenhet.

För att angripa dessa problem är mitt arbete baserat på parameteruppskattning och modellval via nested sampling, samt neurala nätverk för maskininlärning. Med hjälp av avancerade Bayesianska metoder har jag satt gränser på egenskaperna hos halor av mörk materia längs med supernovors siktlinjer via deras svaga gravitationella effekt, utvecklat metoder för fotometrisk klassificering av supernovor från deras ljuskurvor, samt arbetat med mera allmänna frågor associerade med bestämningen av de kosmologiska parametrarna samt undersökt förenligheten av olika sammanställningar av supernovor.

List of accompanying papers

Paper I M.C. March, N.V. Karpenka, F. Feroz and M.P. Hobson.

Comparison of cosmological parameter inference methods applied to supernovae lightcurves fitted with SALT2, MNRAS **437**, 4 (p. 3298-3311); [arXiv:1207.3705](#).

Paper II N.V. Karpenka, M.C. March, F. Feroz and M.P. Hobson.

Bayesian constraints on dark matter halo properties using gravitationally-lensed supernovae, MNRAS **433**, 4 (p. 2693-2705); [arXiv:1207.3708](#).

Paper III N.V. Karpenka, F. Feroz and M.P. Hobson.

A simple and robust method for automated photometric classification of supernovae using neural networks, MNRAS **429**, 2 (p. 1278-1285); [arXiv:1208.1264](#).

Paper IV N.V. Karpenka, F. Feroz and M.P. Hobson.

Testing the mutual consistency of different supernovae surveys, submitted to MNRAS; [arXiv:1407.5496](#).

Paper V N.V. Karpenka, F. Feroz and M.P. Hobson.

Photometric classification of supernovae using hierarchical neural network method, to be submitted to MNRAS.

Acknowledgments

I thank my supervisor, Prof. Joakim Edsjö, for his advice and support, and for allowing me the academic freedom to pursue a diverse range of projects.

I thank all the people who have been a part of the fantastic OKC family during my PhD years; it is impossible to name you all. Thank you for the lunch chats, Tuesday fikas, coffee breaks, poker nights and midsummer, New Years and the other celebrations we shared. And a little cheeky thanks to Chris Savage for all the time you wasted on teaching me basic programming during my first year.

Another amazing academic family whom I thank is the Cavendish Astrophysics group. Your tea-times in the old tea room and the new tea corridor will stay with me forever. Thanks for making me feel so at home during all my long visits. A special thank you goes to Karen, who made my visits so easy by taking care of all the arrangements. I cannot thank Michael Hobson and Farhan Feroz enough for everything I have learned from them over the last few years; thank you for making me part of the Bayesian club. Farhan, thank you for introducing me to the “giant puri”; my life was incomplete without it! Michael, I could not think of a better mentor and friend than you are to me. The Collison family is also an inseparable part of my Cambridge experience; thanks for your incredible hospitality and all the wine I drank at your house.

I thank my friends from home for visiting me in Stockholm so often and for bringing part of home with them to me, when I didn’t have the chance to go there myself, especially Tanya, Chris, географу-строителю Zhenya and “всем теоретикам”. Talking of home, I give huge thanks to two women, the first of whom gave a solid base to my physics knowledge and the second of whom taught me English and in so doing opened up a whole new world for me. Natallia Dmitrievna Emelyanchenko and Svetlana Vasil’evna Luzgina, I would never have had the chance to complete this work without you!

My dearest thanks go to Johannes. It was a great pleasure to have you in my life for all these years; we lived together, we learned together, and we even

raised a fantastic Weakly Interacting Massive Katt Type A (Wimka) together. It would have been so different without you! I also thank Johannes' family: pappa Pontus, Gisela, mormor Hilde, Charles, Majsan, Elsa, Sabine and everyone else — tack så mycket.

Last, but not least, my thanks go to my family for always being there for me. Babushka Nina, dedushka Misha, and all my aunts, cousins and nephews, thank you for following my successes and for never really asking what it is that I do at work. Mama and Papa, you have always been the greatest example of academics, couple and family for me. I still can't believe my luck that I am your daughter.

Preface

Thesis plan

This doctoral thesis consists of two major parts: (i) a short summary of SN observations, cosmological constraints, the statistical methods used for these analyses and my results; and (ii) the corresponding 5 articles published, submitted or ready to be submitted for publication.

The first part of the thesis is further divided into seven chapters, the contents of which are briefly summarised below.

- * Chapter 1 motivates this work from a cosmological point of view. It gives a short introduction to the history of cosmology, highlights its major discoveries and outlines remaining significant challenges.
- * Chapter 2 gives an overview of the numerical methods used in my work: Bayesian methods and their use in parameter estimation and model selection; scanning algorithms, concentrating on MULTINEST; and neural networks (NNs) and their applications.
- * Chapter 3 discusses SN discovery, classification and the study of progenitor models. It presents a historical overview of SN surveys and an outlook on the current state and problems that future surveys will bring. It also summarises the techniques for the standardisation of SNIa, and their associated shortcomings.
- * Chapter 4 discusses different techniques, including the χ^2 -method and Bayesian Hierarchical Method (BHM), for cosmological parameter inference, and an assessment of their advantages and drawbacks.
- * Chapter 5 reviews gravitational lensing effects in astronomy; it gives a short derivation of the lens equation and shows how one can view SNe through gravitational telescopes.

- * Chapter 6 summarises the main results in my papers and unpublished studies.
- * Chapter 7 gives a brief outlook on future challenges in SN cosmology and outlines, in this context, how one can develop further the methods presented in this work to address these issues.

My contribution to the papers

Paper I

I made the original discovery of the previously unknown difference in the best-fit cosmological parameters obtained from the 3-year SuperNova Legacy Survey (SNLS) SN catalogue using the standard χ^2 -method and the BHM. I initiated the project to explore this difference systematically, using SN simulations as well as real SN data. I worked closely with Marisa March in interpreting the results and led numerous discussions regarding the direction of the project and the content of the paper. I also wrote and revised large sections of the manuscript.

Paper II

I proposed the project to perform a Bayesian analysis of gravitationally-lensed SNe to constrain the properties of dark matter haloes along their lines-of-sight. I wrote the code to perform the simulations and the analysis of real data. I ran the code and performed the numerical calculations to produce the results, made the plots for the paper and wrote most of the manuscript.

Paper III

I suggested the original idea of creating a homogeneous training set by fitting SN lightcurves with a parameterised function. I wrote the code to perform this fitting and ran it to produce the training sets and plots of the fits. I interpreted the results of the NN classifier and led discussions regarding the direction of the research and the content of the paper. I wrote most of the manuscript.

Paper IV

I created the realistic simulations. I wrote the code used for the analysis of the simulations and real data. I also interpreted and summarised all the results. I created all the plots used in the paper. I wrote most of the manuscript.

Paper V

I created the data-sets for the hierarchical NN (HNN) training. I interpreted the results of the NN classifier. I created all the plots of the paper. I wrote most of the manuscript. I simulated realistic Dark Energy Survey (DES) data-sets to investigate this method further.

Natallia V. Karpenka
Stockholm, August 2014

List of abbreviations

BHM	Bayesian Hierarchical Method
CCD	charge-coupled device
CDM	cold dark matter
CMB	cosmic microwave background
CSP	Carnegie Supernova Project
DES	Dark Energy Survey
HNN	hierarchical neural network
HST	Hubble Space Telescope
HZT	High-Z team
MCMC	Markov chain Monte Carlo
MLCS	Multi Light Curve Shape
NFW	Navarro–Frenk–White
NN	neural network
iPTF	intermediate Palomar Transient Factory
SALT	Spectral Adaptive Lightcurve Template
SCP	Supernova Cosmology Project
SDSS	Sloan Digital Sky Survey
(t)SIS	(truncated) singular isothermal sphere
SLSN	superluminous supernova
SN	supernova
SNIa	supernova type Ia
SNII-P	Type II Plateau SN
SNLS	SuperNova Legacy Survey
WMAP	Wilkinson Microwave Anisotropy Probe
ZTF	Zwicky Transient Factory

Contents

Abstract	v
Svensk sammanfattning	vii
List of accompanying papers	ix
Acknowledgments	xi
Preface	xiii
List of abbreviations	xvii
Contents	xix

I Background material and summary of my results	1
1 Introduction	3
1.1 Relativistic gravitation, cosmology and the expanding universe	3
1.2 Cosmic structure and dark matter	7
1.3 Gravitational lensing	10
1.4 SNe, universal acceleration and dark energy	11
1.5 Inflation, uncertainty and the future	12
2 Statistical methods	15
2.1 Bayesian statistics	16
2.1.1 Check for inconsistency between data-sets: the \mathcal{R} -test	17
2.1.2 Analysis of potentially inconsistent data-sets: hyper-parameters	18
2.2 Nested sampling and the MULTINEST algorithm	19

2.3	Machine-learning and neural networks	23
3	SNe: from sky to catalogue	27
3.1	Observational techniques	28
3.1.1	Photometry	28
3.1.2	Spectroscopy	29
3.1.3	Near-infrared observations	29
3.2	Classification	29
3.3	Searching for SNe	31
3.3.1	Finding events	32
3.3.2	Follow-up observations	32
3.3.3	Surveys	33
3.4	SN Ia	36
3.4.1	Explosion models	37
3.4.2	SN lightcurves	37
3.4.3	Standardization of SNe	39
3.5	Type non-Ia SNe in cosmological analyses	41
4	Cosmological parameter inference using SNe	43
4.1	Comparing theory and observations	44
4.2	Toy simulations of SN data	46
4.3	Naive definition of the likelihood	47
4.4	The standard χ^2 -method	48
4.5	BHM	51
4.6	Generalised Bayesian Likelihood	55
5	Gravitational lensing of SNe	59
5.1	Lens equation	59
5.2	Types of gravitational lensing	61
5.3	SNe through gravitational telescopes	62
6	Summary of my results	65
6.1	SNe and cosmology	65
6.1.1	Biases in the χ^2 -method and BHM	66
6.1.2	BHM with redshift-dependent stretch and colour corrections	67
6.2	SNe and cosmic structure	68
6.2.1	SIS model	69
6.2.2	NFW model	71

6.2.3	Model selection between different dark matter halo models	73
6.2.4	Foreground galaxies catalogue	75
6.3	SNe photometric classification	76
6.3.1	First step: Lightcurve fitting	76
6.3.2	Second step: NN classification	77
6.3.3	SuperNova Photometric Classification Challenge (SNPCC)	78
6.4	Testing consistency	80
6.4.1	Consistency test based on χ^2 -method	80
6.4.2	Consistency test based on BHM	81
6.4.3	Hyper-parameters	82
7	Outlook	85
7.1	Future problems for SN astronomy	85
7.2	My interest for the coming years	86
A	Princes cake	89
A.1	Ingredients	89
A.2	What to do	90
A.3	When to eat	91

Part I

Background material and summary of my results

Chapter 1

Introduction

‘You never know when you’ll luck out. Take it from one who knows.’

Max Frei

In this chapter, I present a broad introduction to the standard model of cosmology, on which the research presented in this PhD thesis is based. Rather than presenting a detailed analytical description, which can be found in numerous textbooks, I present a more qualitative, chronological account of its development, which hopefully makes this material more accessible and places into context how we have arrived at our current understanding of the Universe. The original research in this thesis is focussed on observations of SNe and the application of novel statistical methods to their analysis, and I will describe these topics in subsequent chapters.

1.1 Relativistic gravitation, cosmology and the expanding universe

Nearly a century has passed since Einstein published his completed theory of general relativity in November 1915. Within a month, Einstein discovered that his new theory could account precisely for a well-known “anomaly” in the orbit of Mercury. Moreover, in 1919, his prediction for the deflection of light from distant stars by the Sun was experimentally verified by Arthur Eddington, and Einstein became internationally famous.

As early as 1917, Einstein realised that he had the necessary tools with which to derive the first fully self-consistent model of the Universe as a whole. He immediately faced a problem, however, in that his equations predicted the Universe

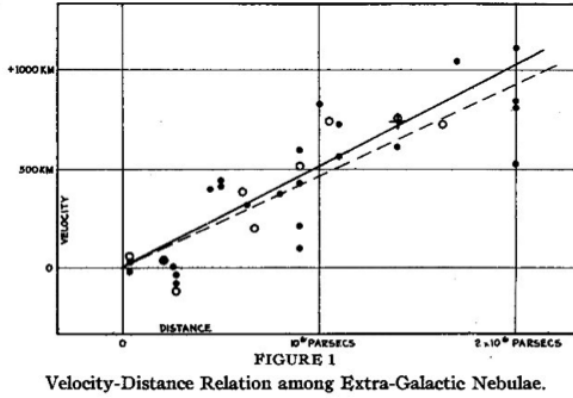


Figure 1.1: Plot from Hubble (1929), which shows that the redshift of a galaxy, interpreted by Hubble as a speed of recession, is proportional to its distance.

to expand or contract, which ran contrary to the prevailing belief at the time that the Universe was static. In order to construct a static model for the Universe, Einstein added to his equations an extra term that contained a new constant of nature called the “cosmological constant”. By carefully fine-tuning the value of the cosmological constant, Einstein constructed a static model of the Universe. Through the mid 1920s, however, Friedmann, Lemaître and Robertson all independently obtained the general solution to Einstein’s equations of general relativity for an isotropic universe, each finding that, without fine-tuning the value of the cosmological constant, the generic predicted behaviour was for the universe to expand or contract.

Theory and observation came together in 1929, when Edwin Hubble combined his distance estimates to a selection of spiral galaxies with exquisite spectroscopic studies of the galaxies made nearly 20 years earlier by Vesto Slipher. Such spectra may be used as a cosmic “bar-code” to identify particular atoms from the pattern of narrow lines in the spectrum, and also as a “radar-gun” to determine the velocity of the emitting material along the line-of-sight by measuring the Doppler shift in the wavelength of the spectral lines as compared with laboratory measurements on Earth. Slipher found that the “spiral nebulae” were made from normal matter, but also discovered that their observed spectral lines were all shifted significantly to longer wavelengths (towards the red end of the visible spectrum of light). From these so-called “redshifts” in the spectral lines¹,

¹The redshift z is defined by $1 + z = \lambda_{\text{obs}}/\lambda_{\text{em}}$, where λ_{obs} is the observed wavelength of the spectral line and λ_{em} is its emitted wavelength, i.e. that measured in a laboratory experiment.



Figure 1.2: Eight-year-old artists' impressions of the Big Bang. Photograph courtesy of Pontus Bergström.

he thus deduced that the galaxies were all moving away from us at considerable speeds. When Hubble compared the speeds of recession of these galaxies with the distances that he had measured to them, obtained by observing the periods of the Cepheid variable stars that they contained, he made the astonishing discovery that the speed of recession of an object is proportional to its distance, as shown in the Figure 1.1. This was interpreted as resulting from the Universe expanding uniformly in all directions. When Einstein learned of Hubble's results, he is said to have described his inclusion of the additional cosmological constant term in the equations of general relativity as “the biggest blunder” of his life. As we will see later, however, posterity may judge otherwise.

The expansion of the Universe, when combined with Einstein's theory of general relativity (with the simplifying assumptions of the large-scale homogeneity and isotropy of space) laid the foundations for the development of the standard Big Bang theory of cosmology (Figure 1.2), which remains to the present day our best description of the Universe. The idea was first proposed in 1932 by Georges Lemaître, who suggested that the observed expansion of the Universe implied that, moving backwards in time, it must contract and would continue to do so until all the matter in Universe was contained in a single point, a “primeval atom”, which marked the origin of the spacetime fabric itself. Thus, running the expansion of the Universe backwards according to the laws of general relativity, and extrapolating, implies that the matter had an infinite density and temperature at a *finite* time in the past. Indeed, the presence of such a *singularity* indicates the limit of applicability of the theory of general relativity.

Based on a range of cosmological observations, it is currently estimated that this occurred around 13.7 billion years ago. It is worth noting, however, that the Big Bang theory cannot and does not provide any explanation for the initial singularity, but instead describes and explains the general evolution of the Universe since that instant, as it expanded from an extremely hot and dense state at very early times to its cool and diluted state today.

The Big Bang theory was advocated and developed further in the late 1940s and early 1950s by George Gamow, who introduced the idea that the nuclei of the light elements, such as helium, deuterium and lithium, could be formed from nuclear processes occurring in the rapidly expanding and cooling first minutes of the Universe, following the Big Bang. His colleagues, Ralph Alpher and Robert Herman, also determined the thermal history of the Universe in this model and predicted the existence of the cosmic microwave background (CMB) radiation, a near-uniform bath of thermal radiation, sometimes called “the afterglow of creation”, that pervades the Universe. Alpher and Hermann calculated that, just 300,000 years after the Big Bang, the Universe would cool sufficiently for the ionised gas of mostly free protons and electrons (plus other light nuclei) to combine to form neutral atoms (predominantly hydrogen), marking a sharp transition between an opaque charged-particle plasma to a transparent neutral gas through which photons can travel unhindered, stretching as the Universe expands, until they are observed today as the CMB, a thermal blackbody radiation characterised by a temperature of just a few Kelvin.

By the early 1960s, observations also revealed that the percentage by mass of Helium in the Universe was around 23%. This uniformity and the fact that this percentage was much greater than what could be created in the cores of stars pointed to a cosmic origin, as suggested earlier by Gamow. Hoyle showed that such a percentage of Helium was indeed predicted to be synthesised in the early stages of the Big Bang. Subsequent calculations by Fowler and Wagoner showed that Big Bang nucleosynthesis also produced traces of other light elements, which were very difficult to form inside stars. The predicted abundances matched observations very well. The status of the Big Bang as our best theory for the origin and evolution of the cosmos was secured, however, by the serendipitous discovery of the CMB by Penzias and Wilson in 1964. While preparing the 20-foot horn-shaped antenna at Bell Laboratories to perform some radio-astronomical observations, they discovered an excess of radiation at a temperature of around 3 Kelvin, wherever they pointed the telescope in the sky. After exhaustive efforts to find the source of this emission, which even included scraping out bird droppings from the inside of the antenna, Penzias and Wilson realised that the signal must be the CMB predicted by Alpher and Hermann.

Indeed, this oldest light in the Universe has since proven to be a great gift to cosmology, since it provides an early-childhood snapshot of the Universe when it was just a tiny fraction of its current age. After the discovery of the CMB, and especially when its spectrum was measured to be precisely that of thermal radiation from a black body, most cosmologists were persuaded that some version of the Big Bang scenario must have taken place.

1.2 Cosmic structure and dark matter

Since the 1960s, most work in cosmology has been in the context of the Big Bang model, and devoted in particular to understanding how large-scale structure in the Universe, such as galaxies and clusters, form in the context of the Big Bang model. This has led to many surprises and, at times, considerable scepticism in the standard Big Bang theory, which has had to evolve considerably to match increasingly accurate observations. Most notably, it has proven necessary to postulate the existence of a new form of matter that interacts only gravitationally with normal baryonic matter and is hence invisible: dark matter.

The earliest evidence suggesting the existence of dark matter came instead from observations of the distributions of velocities of the galaxies within galaxy clusters. In 1933, Zwicky noticed that outer members of the Coma cluster are moving far too quickly to be merely tracing the gravitational potential of the visible cluster mass. In order to make the observed velocities consistent with the virial theorem, one needed to postulate that the cluster also contained additional matter, which could not be seen. Observations by Babcock in 1939 showed that this was also the case on the scale of the individual galaxy Andromeda. More extensive observations by Rubin and Ford during the 1960s and 1970s of the rotation curves of numerous edge-on spiral galaxies observed clearly showed that the (near) circular velocities of their constituent stars as a function of distance from the centre of the galaxy remain approximately constant out to the observable extent of the galactic disc. This is in stark contrast to the expected fall-off in circular velocities expected from the visible matter contained within the stars' orbits, and suggests the presence of a large dark matter "halo" in which the visible galaxy is embedded.

The main argument for dark matter comes, however, from the central problem for the original Big Bang model to explain the formation of galaxies. As early as the 1930s and 1940s, Lemaître, Tolman and Lifshitz all independently showed that density perturbations in an expanding universe grow quite slowly under their own self-gravity, with their density contrast relative to the background increasing only in proportion to the growth of the overall scale factor of

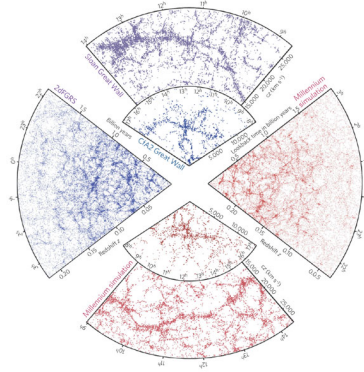


Figure 1.3: Top panel present the CfA2 “Great Wall”, centered on the Coma cluster and to the left is one-half of the 2dFGRS, which represents real measurements. Bottom and right panels present simulations constructed using “the Millennium” simulation and uses geometries and magnitude limits matching corresponding surveys. Credit: [Springel, Frenk, & White \(2006\)](#).

the universe. Assuming galaxies evolved from infinitesimal density fluctuations in the very early Universe, they inferred that galaxies could not have formed by the current epoch, which is clearly contrary to observations, which in the 1950s and 1960s began to uncover the large-scale distribution of galaxies and clusters in the Universe through the work of Neyman, Abell and Zwicky. Moreover, in the 1960s and 1970s, a number of theoretical cosmologists, including Harrison, Zel’dovich, Peebles and Silk, had shown that to form these galaxies and clusters, the small density perturbations from which they evolved should leave imprints in the temperature distribution of the CMB across the sky. By 1980, however, the predicted amplitude of these temperature fluctuations exceeded observational limits on anisotropies in the CMB and clearly a fundamental change was needed in our understanding of the formation of structure in the Universe. This led the theoretical cosmologist Jim Peebles to suggest that the Universe might be dominated by a hitherto unknown form of matter, now called dark matter, that interacts only very weakly with normal (baryonic) matter, of which we and everything we see around us is comprised. This allows for dark matter fluctuations to form, into which normal matter can later “fall”, without imprinting excess temperature variations in the CMB.

Detailed numerical simulations showed this model to be remarkably successful in accounting for the large-scale distribution of structure in the Universe (Figure 1.3). On large scales, galaxies are collected into clusters, clusters are part of superclusters, and superclusters are arranged into large-scale

sheets, filaments and voids. According to cosmological “N-body” simulations (e.g. Navarro et al. 1996; Springel et al. 2005; Diemand et al. 2007; Springel et al. 2008; Diemand et al. 2008), the formation of the observed large-scale structure of luminous matter could only have taken place in the presence of a substantial amount of dark matter. In addition, most of the dark matter has to be both cold and non-dissipative to enable the production of the observed structures. “Cold” in this context means that it moves non-relativistically, and thus has a short free-streaming length (for example, smaller than the size of a gas cloud undergoing gravitational collapse). Being cold implies that the dark matter can gravitationally aggregate on small scales and hence seed the formation of galaxies, as mentioned above, while being non-dissipative prevents it from cooling and collapsing with the luminous matter and overproducing galactic discs.

Most importantly, when the Cosmic Background Explorer satellite detected anisotropies in the CMB for the first time in 1992, they were found to be at a level of about one part in 100,000 relative to the 2.73 Kelvin background, which is consistent with structure formation in the cold dark matter (CDM) scenario. During the following decade, the CMB anisotropies were measured with increasing accuracy by a large number of ground-based and balloon-borne experiments, by the Wilkinson Microwave Anisotropy Probe (WMAP) satellite over the period 2002-2009, and most recently by the Planck satellite, which completed its observations in 2013. All these observations remain consistent with the CDM model. Moreover, the power in the CMB anisotropies measured on different angular scales is consistent with the observed large-scale correlations in the distribution of galaxies. This observation of Baryon Acoustic Oscillations (Albrecht et al. 2006) strongly supports the idea that cosmic structure formed from the passive gravitational collapse of primordial density perturbations, the imprints of which we see in the CMB.

Indeed, CMB observations can be combined with independent measurements of $\Omega_{b,0}$ (the present-day baryonic matter density) and $\Omega_{m,0}$ (the present-day total matter density) from Big Bang nucleosynthesis and large-scale structure observations, respectively, to provide very strong evidence for the existence of dark matter. Using the latest Planck results, one obtains posterior mean values and 68 per cent credible intervals of $\Omega_{m,0} = 0.314 \pm 0.020$, $\Omega_{b,0}h^2 = 0.02207 \pm 0.00033$, $\Omega_{dm,0}h^2 = 0.1196 \pm 0.0031$, indicating that dark matter must be predominantly non-baryonic.²

²The present-day density parameter for the i th component is defined as $\Omega_{i,0} = 8\pi G\rho_{i,0}/(3H_0^2)$, where $\rho_{i,0}$ is its physical density and $H_0 \equiv 100h$ is the present-day value of the Hubble parameter, which is estimated to be $H_0 = 67.3 \pm 1.2$ from combined cosmological probes (Planck Collaboration et al. 2013).

1.3 Gravitational lensing

A striking visual representation of the presence of dark matter and a beautiful illustration of general relativity is provided by gravitational lensing. General relativity predicts that light rays are bent around massive bodies or, more generally, undergo deflections when they traverse a region in which the gravitational field is inhomogeneous. In this manner, light from background objects can be “lensed” by massive objects in the foreground as the path of light passing through the gravitational field of foreground object is bent. The deflection of light is not just a relativistic effect, but is also predicted by Newton’s theory of gravitation, when one considers light to be made up of a stream of particles. The Newtonian approach does, however, predict only one-half of the deflection predicted by general relativity. In the latter theory, a light beam that just grazes the surface of the Sun suffers a deflection of 1.75 arcseconds, whereas Newton’s theory predicts just 0.87 arcseconds. Indeed, as I mentioned previously, the observational confirmation of the larger value by Eddington in 1919 was a key factor in leading the scientific community to accept Einstein’s description of gravity in terms of general relativity.

Very massive astronomical objects, which lie at large distances from the Earth, can exert such a strong gravitational effect on light rays that pass near them that a single background source can be observed as multiple images. This phenomenon was predicted very early on in the study of gravitational lensing, but was only observed for the first time in 1979 (Walsh et al. 1979), since when gravitational lensing has become a major area of research in astrophysics. Systems which have been observed to contain multiple images are many tens in number. Of greatest interest to astrophysics is that the analysis of the distribution and shape of these multiple images can be used to derive an accurate estimate of the mass distribution in the lensing object. In particular, when light from distant galaxies is lensed by a cluster, one can see evidence of significant gravitational lensing, far more than can result from the observed distribution of luminous matter in the foreground cluster, thereby implying the presence of dark matter (e.g. Tyson et al. 1998; Massey et al. 2007). Figure 1.4 shows an example of such a cluster.

In most cases, however, the effects of gravitational lensing are far more subtle. Typically, the size and shape of background objects are only very slightly changed. The nature of this change is very difficult to determine for individual objects, since one does not know a priori its unlensed intensity distribution. One therefore has to average the effect of a large number of background objects to obtain a statistical measure of this weak-lensing signal. Indeed, such observa-

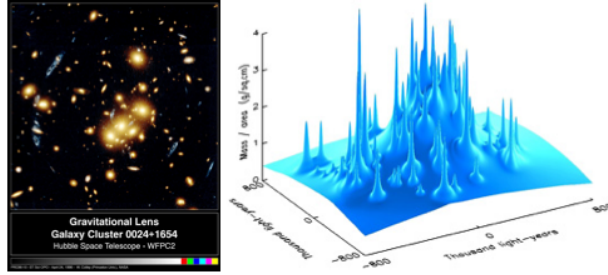


Figure 1.4: Presented in the left panel is an image of a gravitationally lensed cluster, while on the right is the mass map of the foreground cluster. Credit: Greg Kochanski, Ian Dell’Antonio, and Tony Tyson (Bell Labs, Lucent Technologies).

tions can be used to investigate the nature of cosmic structures, provided one has a large collection of lensed background objects to analyse.

1.4 SNe, universal acceleration and dark energy

In the last two decades, there has been an unexpected twist in the story of cosmology. In 1998, measurements of the redshift–magnitude relation for SNIa, which can be used as “standard candles” in cosmology, indicated that, when the Universe was around half of its present age, its expansion underwent a transition from a decelerating phase into an accelerating one, which continues to the current epoch. This came as a complete surprise, as it was thought that the expansion should decelerate as a result of the attractive gravitational force between all objects slowing down the expansion. To explain an accelerating universe, one has to posit some additional component of the universe, known generically as “dark energy”, which has a large negative pressure and thus leads to a gravitational repulsion. Amazingly, the simplest form for such a component is provided precisely by the additional cosmological constant term (or Λ -term) that Einstein included in his equations of general relativity when trying to build a static universe model, but then rejected as his “biggest blunder” when he learned that the Universe is expanding. The resulting “ Λ CDM” scenario is our best current cosmological model, which describes all existing observations. Indeed, results from WMAP, Planck and other CMB observations, combined with galaxy surveys of large-scale structure are all consistent with a Λ CDM model, known as the “concordance cosmology”, in which the total mass/energy density budget

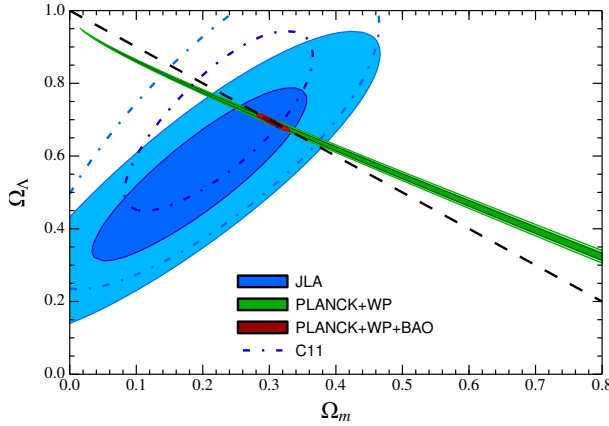


Figure 1.5: 68% and 95% confidence contours for the present-day cosmological density parameters $\Omega_{m,0}$ and $\Omega_{\Lambda,0}$. Labels for the various data-sets correspond to the [Betoule et al. \(2014\)](#) SNIa compilation (JLA), the [Conley et al. \(2011\)](#) SNIa compilation (C11), the combination of Planck temperature and WMAP polarization measurements of the CMB fluctuation (PLANCK+WP), and a combination of measurements of the baryon acoustic oscillations scale (BAO). The black dashed line corresponds to a flat universe. Credit: [Betoule et al. \(2014\)](#).

of the Universe at the present time is comprised of approximately: 73% dark energy, 23% dark matter and 4% ordinary matter (see Figure 1.5), and in which structure forms from the passive gravitational evolution of scale-invariant perturbations generated (somehow) in the very early Universe.

1.5 Inflation, uncertainty and the future

There remain numerous open questions in cosmology. Indeed, many cosmologists view the current standard model of cosmology with considerable scepticism. In addition to the unknown physical nature of both dark matter and dark energy, which supposedly dominate our Universe, our understanding of fundamental physics is only sufficient to project back to around one ten-billionth of a second after the Big Bang, at which epoch the typical densities and energies of particles are at the limit of what can be reached in the latest particle physics experiments, such as the Large Hadron Collider (e.g. [The ATLAS Collaboration: G. Aad et al. \(2008\)](#); [LHC Higgs Cross Section Working Group et al. \(2011\)](#)). At earlier times, the physics of the Big Bang is subject to considerable speculation and doubt. The most popular current model, known as the theory of

inflation, proposes that, almost immediately following the Big Bang, the Universe underwent a short period of exponential expansion, growing in size by a factor of 10^{27} in just 10^{-33} seconds, during which microscopic quantum fluctuations in the matter fields at the time were stretched to macroscopic scales to generate the seeds of structure formation. Indeed, this mechanism for the origin for all the structure in the Universe was proposed by Guth, Linde and Starobinsky, amongst others, in the early 1980s. The inflationary model also solves a number of other problems, such as explaining why the Universe is so homogeneous and isotropic on the largest scales. Very recent support for the inflationary paradigm has potentially been provided by the BICEP2 experiment ([Ade et al. 2014](#); [BICEP2 Collaboration et al. 2014](#)), which claims to have observed polarised emission from CMB anisotropies that is consistent with the presence of primordial gravitational waves, which are also predicted to be produced (almost exclusively) by inflation. There are currently, however, some concerns regarding the interpretation of the BICEP2 results, and further experimental verification is required.

Although an attractive proposal, inflation does, however, have some theoretical problems of its own. In particular, determining the initial conditions for inflation is both conceptually and technically very demanding, and it may be the case that producing a period of inflation that is consistent with observations requires an unacceptable level of fine-tuning in the theory, but this is far from certain. Thus, cosmology now finds itself again in a period rich in alternative models, the development of which is driven by scepticism in our existing description of the Universe. Only time will tell whether (another) revolution in our thinking is required, but, based on the experience of the last one hundred years, it seems very likely.

Chapter 2

Statistical methods

‘There are three kinds of lies: lies, damned lies, and statistics.’

Benjamin Disraeli

There are two ways to define probability. One of them is Frequentist, which postulates that probability is “the ratio of the times the event occurs in a test series to the total number of trials in the series” (D’Agostini 1995), or the “frequencies of outcomes in random experiments” (Mackay 2003), and the other is Bayesian, which postulates that probability is “a measure of the degree of belief that an event will occur” (D’Agostini 1995). In my research, I choose to follow the Bayesian interpretation of probability, since it provides the only self-consistent extension of Boolean algebra to propositions that are not simply true or false, but are associated with a degree of belief (defined to lie between 0 and 1) (Cox 1946).

On a more practical note, the recent development of efficient sampling algorithms makes the implementation of Bayesian methodology more straightforward and reliable than its Frequentist counterpart. The central reason for this lies in what Bayesians and Frequentists consider to be the most important properties of probability distributions. In contrasting the two statistical schools, much attention is usually paid to the issue of priors. It is indeed true that Bayesians consider the posterior probability, namely the product of the likelihood and the prior, as the primary distribution for inference. By contrast, the Frequentists tend to eschew the notion of priors and concentrate on the likelihood alone. This difference is, however, often overstated and leads practically to very little difference in the final inferences. A far more profound practical difference between the schools is that Bayesians consider probability mass as most important, whereas Frequentists consider the point-value of the probability as primary.

Thus, given a probability distribution (either the posterior or the likelihood), a Bayesian integrates under the distribution to identify regions of the parameter space containing the largest integrated probability, whereas the Frequentist aims to identify the point(s) in the parameter space with the largest probability value, at least when adopting the most commonly-used maximum-likelihood or maximum a posteriori estimators. Using a thermodynamic analogy, Bayesians focus on heat whereas Frequentists concentrate on temperature. This difference between the schools is far more fundamental than the use of priors, and has immediate practical consequences. By obtaining Monte Carlo samples from the distribution, the construction of marginal probability distributions, as preferred by the Bayesian, is far more easily and reliably achieved than the construction of profile likelihoods, as preferred by the Frequentist. This provides another, very practical reason for choosing the Bayesian approach.

2.1 Bayesian statistics

In general, the probability $\Pr(A|B)$ is the degree of belief, given B , of the truth of A . *Bayes' theorem* can be used to change the order of the conditioning,

$$\Pr(A|B) = \frac{\Pr(B|A) \Pr(A)}{\Pr(B)}. \quad (2.1)$$

In many cases, one wants to use a set of observations or data to infer values of parameters within a given model. Given a model or hypotheses H with a set of N free parameters $\Theta = \{\Theta_i\}$, together with a data-set \mathbf{D} , Bayes' theorem implies that one can write

$$\Pr(\Theta|\mathbf{D}, H) = \frac{\Pr(\mathbf{D}|\Theta, H) \Pr(\Theta|H)}{\Pr(\mathbf{D}|H)}, \quad (2.2)$$

where $\Pr(\Theta|\mathbf{D}, H)$ is the posterior probability (density) of the parameters Θ , $\pi(\Theta) \equiv \Pr(\Theta|H)$ is the prior probability (density), $\mathcal{L}(\Theta) \equiv \Pr(\mathbf{D}|\Theta, H)$ is the probability (density) of the data \mathbf{D} , for assumed parameter values Θ (called the likelihood when considered as a function of Θ), while $\Pr(\mathbf{D}|H)$ is the *Bayesian evidence*,

$$\mathcal{Z} \equiv \Pr(\mathbf{D}|H) = \int \Pr(\mathbf{D}|\Theta, H) \Pr(\Theta|H) d^N \Theta = \int \mathcal{L}(\Theta) \pi(\Theta) d^N \Theta. \quad (2.3)$$

Note that this makes the posterior in Eq. 2.2 normalised to unity over the space of parameters.

In parameter estimation, the complete Bayesian inference is embodied in the posterior distribution of the parameter values. This may be used to obtain joint constraints on all parameters simultaneously or constraints on individual parameters by the process of integrating out (or marginalising over) all the other parameters. In practice, the posterior distribution is explored by drawing samples from it using (most often) standard Markov chain Monte Carlo (MCMC) sampling techniques. Once they have reached equilibrium, such methods produce a set of samples whose density is proportional to the posterior. In the entire process, one need not calculate the evidence to normalise the posterior, since the evidence does not depend on the parameters.

By contrast, the evidence is the key quantity of interest for the problem of model selection. Since the evidence may be considered as the average of the likelihood over the prior, it provides a natural means of applying Occam's razor. If a model has a highly-peaked likelihood, but there exist large regions of the parameter space that are disfavoured, since the likelihood is low there, then the evidence of the model will be small. Large evidence values occur for models for which a large fraction of the allowed parameter space is likely. Thus, one can decide which of two models H_0 and H_1 is preferred by the data \mathbf{D} by calculating the ratio of posterior probabilities

$$\frac{\Pr(H_1|\mathbf{D})}{\Pr(H_0|\mathbf{D})} = \frac{\Pr(\mathbf{D}|H_1) \Pr(H_1)}{\Pr(\mathbf{D}|H_0) \Pr(H_0)} = \frac{\mathcal{Z}_1 \Pr(H_1)}{\mathcal{Z}_0 \Pr(H_0)}, \quad (2.4)$$

where $\Pr(H_1)/\Pr(H_0)$ is the *a priori* probability ratio for the two models. In most problems this prior ratio is set to unity, but there are cases, most notably in object detection, where one must set this prior ratio quite carefully to offset the “look elsewhere” effect. One uses Jeffreys' scale given in Table 2.1 to interpret the ratio in Eq. 2.4.¹ In practice, the evidence may also be evaluated using MCMC sampling methods, although the standard technique of thermodynamic integration (Ó Ruanaidh & Fitzgerald 1996) typically requires about an order of magnitude more samples than needed for parameter estimation.

2.1.1 Check for inconsistency between data-sets: the \mathcal{R} -test

A useful application of Bayesian model selection is in determining whether different data-sets are mutually consistent. In principle, one should always check that this is the case before performing a joint analysis using them, although

¹Throughout this work, $\log x$ (i.e. without any subscript) denotes the natural logarithm of x , which is also commonly denoted by $\ln x$.

in practice such a check is not often undertaken. Indeed, the vast majority of analyses in SN cosmology do not test whether different surveys are mutually consistent before combining them in a joint analysis to determine cosmological parameters.

Adopting a Bayesian model selection approach, we denote by H_0 the (null) hypothesis that the data-sets are mutually consistent. In this case, one would expect each data-set to prefer broadly the same region(s) of the model parameter space. Under the (alternative) hypothesis H_1 that the data-sets are mutually inconsistent, one or more of them favour a different region (or regions) of the parameter space. Simply performing a joint in this case could lead to erroneous results (see, for example, Appendix A in [Feroz et al. 2008](#) for a demonstration).

In order to determine which one of these hypotheses is favoured by the data, one can perform Bayesian model selection between H_0 and H_1 . Using Eq. 2.4 and assuming that hypotheses H_0 and H_1 are equally likely *a priori*, this can be achieved by calculating

$$\mathcal{R} = \frac{\Pr(\mathbf{D}|H_0)}{\Pr(\mathbf{D}|H_1)} = \frac{\Pr(\mathbf{D}|H_0)}{\prod_i \Pr(D_i|H_1)}. \quad (2.5)$$

Here the numerator represents the standard joint analysis of all the data-sets $\mathbf{D} = \{D_1, D_2, \dots, D_n\}$, whereas the denominator in the final expression represents the case in which each data-set is analysed separately. It is worth noting, however, that the second equality in Eq. 2.5 is valid only when one allows for potential inconsistencies in the preferred values of the *full* set of model parameters. Nevertheless, there are often situations where one is interested only in potential inconsistencies in the preferred values of some *subset* of the model parameters. In such cases, one must use only the first equality in Eq. 2.5 and calculate the denominator $\Pr(\mathbf{D}|H_1)$ by performing a joint analysis of \mathbf{D} in which each data-set is assigned its own “private copy” of only those parameters in the subset of interest. It is clear from Eq. 2.5 that an \mathcal{R} -value larger than unity (or, equivalently, a positive $\log \mathcal{R}$ -value) indicates that the (null) hypothesis H_0 , that all the data-sets are mutually consistent, is favoured. Otherwise, the (alternative) hypothesis H_1 is preferred, indicating some inconsistency between the data-sets. One uses Jeffreys’ scale given in Table 2.1 to interpret the value of \mathcal{R} .

2.1.2 Analysis of potentially inconsistent data-sets: hyper-parameters

One method for accommodating potentially inconsistent data-sets in a joint analysis is to introduce hyper-parameters that effectively assign a weight to each

$\log(\text{odds})$	odds	$\Pr(H_1 \mathbf{D})$	Interpretation
< 1.0	$\lesssim 3 : 1$	$\lesssim 0.75$	Inconclusive
1.0	$\simeq 3 : 1$	$\simeq 0.75$	Weak evidence
2.5	$\simeq 12 : 1$	$\simeq 0.92$	Moderate evidence
5.0	$\simeq 150 : 1$	$\simeq 0.993$	Strong evidence

Table 2.1: Jeffreys’ scale for the interpretation of Bayes factors and model probabilities. The posterior model probabilities for the preferred model are calculated by assuming only two competing hypotheses.

data-set that is determined directly by its own statistical properties (Hobson, Bridle, & Lahav 2002). The space of hyper-parameter weights is explored simultaneously with the space of original model parameters to obtain a joint posterior distribution. By marginalising over the original model parameters, one obtains the posterior distribution of the hyper-parameter weights, which may be used to determine if any inconsistencies exist between different data-sets. Conversely, one can instead marginalise over the hyper-parameters to recover the posterior distribution as a function only of the original model parameters. Moreover, calculation of the Bayesian evidence for the data, with and without the introduction of hyper-parameters (which we denote by the hypotheses H_1 and H_0 , respectively), allows us to perform model comparison to determine whether the data warrant the introduction of weights into the analysis.

When analysing multiple data-sets jointly, inferred values of hyper-parameters which depart significantly from unity indicate the presence of some inconsistency. Even in such cases, however, the hyper-parameter approach allows for a robust joint analysis of the data-sets. In particular, marginalisation over the hyper-parameters allows for the resulting posterior distribution of the original model parameters to broaden or even exhibit multi-modality resulting from the preference of different data-sets for different regions of the model parameter space (see Hobson, Bridle, & Lahav 2002 for more details).

2.2 Nested sampling and the MULTINEST algorithm

It is computationally very demanding to evaluate the multidimensional integral in Eq. 2.3. Nested sampling is a Monte Carlo approach, introduced by Skilling

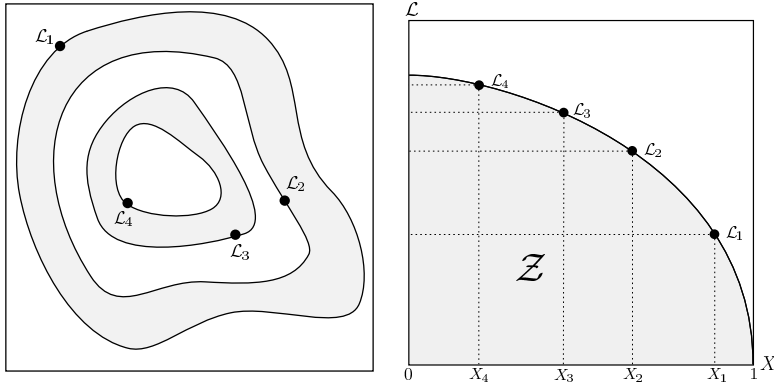


Figure 2.1: Left panel: An example of a two-dimensional posterior distribution. Right panel: The function $\mathcal{L}(X)$. The prior volumes X_i are associated with each likelihood \mathcal{L}_i . Credit: [Feroz & Hobson \(2008\)](#).

(2004), that is designed to calculate the evidence efficiently, and which also produces posterior inferences as a by-product. The method has been extended by [Feroz & Hobson \(2008\)](#) and [Feroz et al. \(2009\)](#), who introduced the MULTI-NEST algorithm, which is able to accommodate posteriors with multiple modes and/or large (curving) degeneracies. In the following description of the algorithm, I will closely follow the discussion given in these two papers.

The key innovation in nested sampling is that the multi-dimensional evidence integral is transformed into a one-dimensional integral. To perform this transformation one first defines the prior volume X via the differential relationship $dX = \pi(\Theta)d^N\Theta$. Thus one can write X as

$$X(\lambda) = \int_{\mathcal{L}(\Theta) > \lambda} \pi(\Theta)d^N\Theta, \quad (2.6)$$

where the domain of integration comprises the region(s) of the parameter space that lies within the iso-likelihood contour $\mathcal{L}(\Theta) = \lambda$. Thus, one can write the evidence integral, Eq. 2.3, as:

$$\mathcal{Z} = \int_0^1 \mathcal{L}(X)dX, \quad (2.7)$$

where $\mathcal{L}(X)$, which is the inverse of Eq. 2.6, is a monotonically decreasing function of X . Thus, the evidence can be evaluated using one-dimensional numerical quadrature integration methods, provided one can evaluate the likelihoods

$\mathcal{L}_i = \mathcal{L}(X_i)$, where X_i is a sequence of decreasing values,

$$0 < X_M < \cdots < X_2 < X_1 < X_0 = 1, \quad (2.8)$$

as shown schematically in Figure 2.1. In particular, one can write the evidence as the weighted sum

$$\mathcal{Z} = \sum_{i=1}^M \mathcal{L}_i w_i, \quad (2.9)$$

where the weights w_i for the simple trapezium rule are given by

$$w_i = \frac{1}{2}(X_{i-1} - X_{i+1}). \quad (2.10)$$

Figure 2.1 gives an illustration of this process for a two-dimensional posterior.

To perform the sum in Eq. 2.9 one begins at iteration $i = 0$ by drawing N samples from the prior distribution $\pi(\Theta)$. These samples constitute the set of so-called “live” or “active” points in the nested sampling process. At this initial stage the volume of the prior is unity, namely $X_0 = 1$. One then calculates the likelihood of each of the active points and determines which of them has the lowest value (which I denote by \mathcal{L}_0); this point is then discarded from the active set. In order to maintain the number of active points, one then replaces the discarded point with a new point that is again drawn from the prior, but is now required to lie within the iso-likelihood contour $\mathcal{L} = \mathcal{L}_0$. The prior volume contained within this contour is not known precisely, since it depends on the points in the original active set. Nonetheless, one may show that the ratio $t = X_1/X_0$ of the new and original prior volumes is distributed as $\text{Pr}(t) = Nt^{N-1}$. As the process continues, the iterative discarding and replacement of the point with the lowest likelihood results in the iso-likelihood contour shrinking and the live points being constrained to ever smaller prior volumes and higher likelihood regions. One may show that after i iterations the prior volume is $X_i \approx \exp(-i/N)$. The process is usually concluded by imposing some criterion on the accuracy to which the evidence has been calculated.

Although nested sampling is designed primarily to calculate the evidence, a happy consequence of the method is that the final set of active points, together with the “historic” set of discarded points produced during the iterations, can be used to obtain posterior inferences on the parameters. Indeed, one may show that posterior-weighted samples are obtained by assigning each point the weight

$$p_i = \frac{\mathcal{L}_i w_i}{\mathcal{Z}}. \quad (2.11)$$



Figure 2.2: The result of applying the ellipsoidal decomposition algorithm in MULTINEST to a set of 1000 points sampled from: two non-intersecting ellipsoids (left panel); and a torus (right panel). Credit: [Feroz & Hobson \(2008\)](#).

Once can then use these samples in the same way as samples obtained from a standard MCMC method to calculate parameter means, standard deviations, and covariances, or even to construct their marginalised posterior distributions.

Nested sampling has been described as only a “meta-algorithm”, since it leaves unanswered the key question of how, at each iteration i , to draw the required replacement point from the prior within the iso-likelihood contour $\mathcal{L} = \mathcal{L}_i$. The MULTINEST algorithm ([Feroz & Hobson 2008](#); [Feroz et al. 2009](#)) performs this task using rejection sampling from a multi-ellipsoidal bound tailored to the current active point set. At each iteration, one performs an expectation-maximisation process to determine the set of (possibly overlapping) ellipsoids that encloses the set of N live points in the minimum volume, subject to the lower limit of the expected prior volume $X_i = \exp(-i/N)$. The new replacement point is then drawn uniformly from the region enclosed by these ellipsoids.

This ellipsoidal decomposition is very flexible and is able to accommodate both multimodal structure and degeneracy lines in the target posterior distribution. In particular, for posteriors that contain well-defined and well-separated modes, the ellipsoidal decomposition allows one to identify the modes and evolve the nested sampling process in each mode separately. In essence, modes are identified as separate entities if there exist ellipsoid(s) set that do not overlap with any others. An illustration of the ellipsoidal decomposition performed by MULTINEST is given in Figure 2.2. More recently, further developments of MULTINEST has been made to enable even more accurate evaluation of the evidence [Feroz et al. \(2013\)](#).

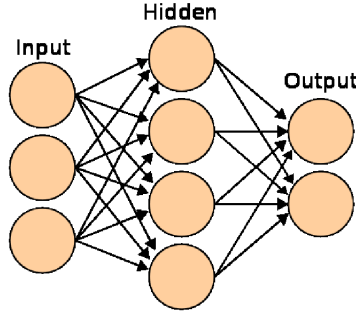


Figure 2.3: A 3-layer NN with 3 inputs, 4 hidden nodes, and 2 outputs. Image courtesy of Wikimedia Commons.

2.3 Machine-learning and neural networks

In addition to performing parameter estimation and model selection using Bayesian methods, in this thesis I also use machine-learning techniques, particularly for the photometric classification of SNe into their respective types (see Section 6.3 and Papers III and V). From the numerous approaches to machine-learning, I use neural networks (NNs). In particular, I employ the SKYNET package, which is a generic NN training algorithm (Graff et al. 2013, 2014).

An artificial NN is a mathematical model loosely based on the structure of the brain. A NN consists of groups of nodes that are connected to one another by directional links that are assigned particular weights. Using these links, each node processes information it receives and then passes the result to other nodes. A great short introduction to NNs is given by Mackay (2003).

In this thesis, I focus entirely on the simplest form of NNs, which are known as feed-forward networks. In particular, I will consider only 3-layer networks, which consist of a layer of input nodes, connected to a “hidden” layer, which itself is then connected to an output layer (see Figure 2.3).

Each node (or perceptron) in the network maps an input vector $\mathbf{x} \in \mathbb{R}^n$ to a scalar output $f(\mathbf{x}; \mathbf{w}, \theta)$ given by

$$f(\mathbf{x}; \mathbf{w}, \theta) = \theta + \sum_{i=1}^n w_i x_i, \quad (2.12)$$

where $\{w_i\}$ and θ are, respectively, the “weights” and “bias” of the perceptron. Thus, for a 3-layer NN, the outputs of the nodes in the hidden and output layers

are (Graff et al. 2012)

$$\text{hidden layer: } h_j = g^{(1)}(f_j^{(1)}); f_j^{(1)} = \theta_j^{(1)} + \sum_l w_{jl}^{(1)} x_l, \quad (2.13)$$

$$\text{output layer: } y_i = g^{(2)}(f_i^{(2)}); f_i^{(2)} = \theta_i^{(2)} + \sum_j w_{ij}^{(2)} h_j, \quad (2.14)$$

where the indices l , j and i indicate, respectively, input, hidden and output nodes, and $g^{(1)}$ and $g^{(2)}$ are called activation functions. It may be shown that, for the NN to operate correctly, these functions must obey certain requirements, namely that they are smooth, monotonic and bounded. I follow Graff et al. (2012) and use $g^{(1)}(x) = \tanh(x)$ and $g^{(2)}(x) = x$.

When one “trains” a NN, one determines the values of the weights and biases that optimise the accuracy of the mapping from the input nodes to the output nodes. The existence of a suitable mapping is guaranteed by the “universal approximation theorem” (Hornik et al. 1990). As one increases the number of hidden nodes, the accuracy of the mapping typically increases, but so does the possibility of overfitting the training data. Nonetheless, the ability of the network to learn complicated mappings may be compromised if the number of hidden nodes is too low. There is therefore a balance between these competing factors and the optimal number of hidden nodes is best determined by comparing the fitting error and correlations of NNs with different numbers of such nodes trained on the same data.

In training a NN, we wish to find the optimal set of network weights and biases (which together we call the network parameters \mathbf{a}) that maximise the accuracy of the predicted outputs. However, one must be careful to avoid overfitting to the training data at the expense of making predictions for input values the network has not been trained on. The general procedure for training a NN is to present it with a set of input and outputs (or targets) $\mathcal{D} = \{\mathbf{x}^{(i)}, \mathbf{t}^{(i)}\}$. Typically around 75% of the set should be used for actual NN training, while the remainder is used as a validation set of data to determine convergence and avoid overfitting.

To train the network, one optimises the probability of reproducing the known training data outputs with respect to the network parameters. For problems of regression (fitting the model to a function), this yields a log-likelihood for \mathbf{a} in the form of a standard χ^2 misfit function, given by

$$\mathcal{L}(\mathbf{a}) = - \sum_{j=1}^{n_{\text{out}}} \log \sigma_j - \frac{1}{2} \sum_{i=1}^{n_t} \sum_{j=1}^{n_{\text{out}}} \left[\frac{t_j^{(i)} - y_j(\mathbf{x}^{(i)}; \mathbf{a})}{\sigma_j} \right]^2, \quad (2.15)$$

where n_t is the number of training data, n_{out} is the number of network outputs, and $y_j(\mathbf{x}^{(i)}; \mathbf{a})$ are the NN's predicted outputs for the input vector $\mathbf{x}^{(i)}$ and network parameters \mathbf{a} . The values σ_j are hyper-parameters of the NN model that describe the standard deviation of each of the outputs.

For a classification network that aims to learn the probabilities that a set of inputs belongs to a set of output classes, the outputs of the network are *softmaxed* to become probabilities,

$$p_j = \frac{e^{y_j}}{\sum_{j'} e^{y_{j'}}}. \quad (2.16)$$

The classification likelihood is then given by the cross-entropy function

$$\mathcal{L}(\mathbf{a}) = \sum_{i=1}^{n_t} \sum_{j=1}^{n_c} t_j^{(i)} \log p_j(\mathbf{x}^{(i)}; \mathbf{a}). \quad (2.17)$$

In this scenario, the true and predicted output values are probabilities. In the true outputs, all are zero except for the correct output class, which has a value of one.

Chapter 3

SNe: from sky to catalogue

‘When he shall die,
Take him and cut him out in little
stars,
And he will make the face of
heaven so fine
That all the world will be in love
with night
And pay no worship to the garish
sun.’

William Shakespeare

Observations of SNe have been recorded since ancient times, transient objects which flare brightly and appear as “new stars” against the unchanging background static stars, only to fade after about a month or so. The term “nova” was first used by Tycho Brahe (1546-1601) to describe a “new star” which appeared in the constellation of Cassiopeia on 11th November 1572, which he observed from Herrevads kloster, Sweden. Much later Fritz Zwicky and Walter Baade differentiated between “two well-defined types of new stars or novae which might be distinguished as common novae and super-novae” (Baade & Zwicky 1934; Zwicky 1940). Nevertheless, only since the late 1990s, in the era of charge-coupled device (CCD) telescopes, have SNe made their contribution to cosmology. After the great success of the Calan–Tololo survey, it became clear that one can successfully standardise multi-band SN data, based on their reproducible luminosities. The story of realisable “standard cosmological candles” had begun.

In this chapter, I discuss SN discovery, classification and the study of progenitor models. I give a short historical overview of past SN surveys, summarise the current state of the field and give an outlook on future surveys. I also summarise the techniques for standardising SNIa, and their associated shortcomings.

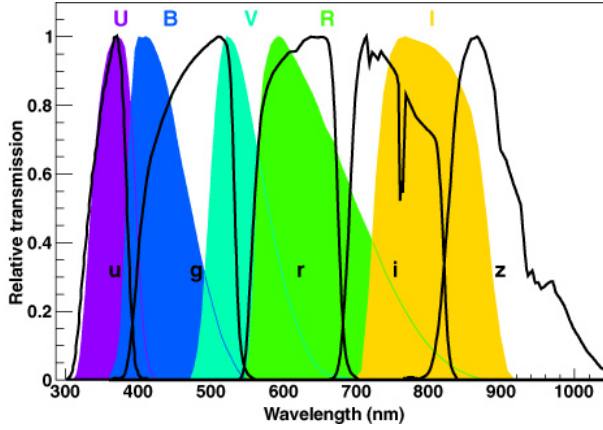


Figure 3.1: Shapes of the commonly used photometric bands in the visible light, arbitrarily normalised. U, B, V, R, I refer to standard bands from [Bessell \(1990\)](#), and u, g, r, i, z to the SDSS bands from [Fukugita et al. \(1996\)](#). Credit: [Astier \(2012\)](#).

3.1 Observational techniques

Since most of the energy output of a SN is in visible light, the main methods for collecting information about them is through photometric imaging and spectroscopy. Most of the studied SNe are usually observed using both these techniques, so it is very useful to remember the rough rule-of-thumb: if the SN has been detected/measured with a telescope of diameter D , then spectroscopic follow-up will typically require a telescope with diameter $2D$.

3.1.1 Photometry

In Figure 3.1, one can see two different sets of filters commonly used in SN imaging. UBVRI is a “standard” set ([Bessell 1990](#)), and u, g, r, i, z is a set of specially designed filters used by the Sloan Digital Sky Survey (SDSS, [Fukugita et al. 1996](#)). Nowadays, imaging in the visible range is made with a silicon CCD with red cutoff $\sim 1.1\mu\text{m}$ and 10^6 pixels per device.

A standard imaging observation is a two step process: (i) several minutes of integration, (ii) ~ 1 minute of read out. The image resolution for ground-based telescopes is below 1 arcsecond full-width-half-maximum and almost one order of magnitude finer in space.

3.1.2 Spectroscopy

For spectroscopic observations, one most frequently uses fiber optics (Gunn, Siegmund, & Mannery 2006) or systems of lenses (de Zeeuw et al. 2000), which are positioned as a narrow slit in the image plane and disperse the light in the perpendicular direction. Modern multi-object spectroscopy instruments can collect data from up to 1000 objects simultaneously. As in photometric observations, putting spectroscopic instruments in space can be very advantageous, since one can use a slit-less spectrometer down to very low sky brightnesses.

3.1.3 Near-infrared observations

Very promising observations of SNe in the near infrared have been made using low band-gap pixelised semiconductor devices, coupled to integrated readout electronics (Hodapp et al. 1996). Making this kind of observation from the ground has problems since: (i) the atmospheric glow rises with wavelength; (ii) there are numerous absorption lines; and (iii) both these effects are not constant in time. Near infrared observations also have a problem with ionizing radiation affecting the sensors.

3.2 Classification

When describing the use of SNe for cosmological parameter inference one usually means SNIa. However, SNe occur in a very broad range of classes, which is still continuing to expand as SNe with previously unseen properties are discovered.

The first of Baade and Zwicky’s SNe had the broad features characteristic of fast moving ejecta, being about 100 times brighter than regular novae and not showing evidence of hydrogen lines. This was a detection of a “type I” SN. Already in 1941, a different class of SNe had been proposed (Minkowski 1941). These “type II” SNe were fainter than those originally discovered and had a hydrogen line in their spectra. In 1985 another unusual SN was detected, this time it was characterised by the absence both of a hydrogen and silicon line. This prompted a separation into subtypes within “type I” SNe: SNIa were defined as events that have silicon and no hydrogen; type Ib display neither silicon nor hydrogen, but have a strong helium line; and type Ic have none of these lines. Figure 3.2 shows the classification scheme for the main SN types. There is a trend to allocate each somewhat unusual SN event to a new pigeonhole. This queerness can be a small variation in the spectra or lightcurves. This should in most cases be resisted, except if there are clear physical grounds for doing so.

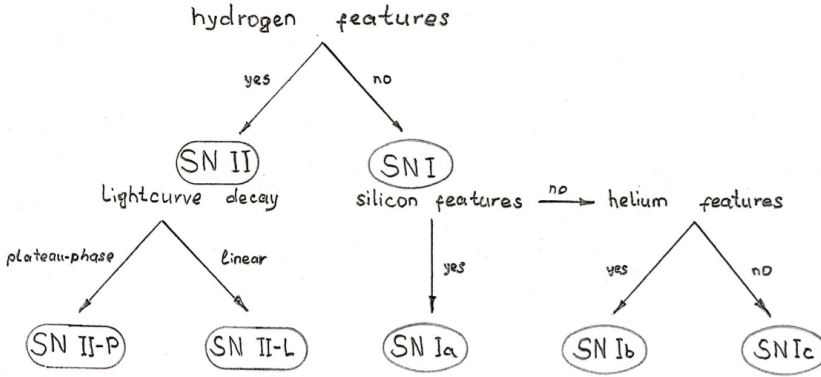


Figure 3.2: SN classification scheme.

Nonetheless, this is sometimes the case. For example, recently a new class of superluminous SNe (SLSNe) have come to light. These SNe are tens to hundreds of times more luminous than “ordinary” SNe, and themselves divide into three subclasses: SLSN-R, SLSN-I and SLSN-II, according to [Gal-Yam \(2012\)](#).

Since SNIa are the main focus of this work, I point out another way of distinguishing between SNIa and non-Ia SNe. SNIa are thermonuclear explosions (see Section 3.4.1), while all the other types are core-collapse explosions.

As mentioned above, the silicon line is a signature of a “standard candle”, which means that in order to distinguish these events from the variety of SN explosions we do need to have spectroscopic measurements. From Figure 3.2 one can see that, indeed, most of the classification is performed on the basis of the presence/absence of some element’s (spectroscopic) lines, but, by contrast, separation within type II is based on the shape of SN lightcurves. Since spectroscopic observations are very “expensive” it would be of great benefit to devise a SN classification method based purely on photometric data (from which one, of course, cannot identify the Si absorption line). Many techniques targeted at SN photometric classification have been developed, mostly based on some form of template fitting ([Poznanski et al. 2002](#); [Johnson & Crots 2006](#); [Sullivan et al. 2006](#); [Poznanski et al. 2007](#); [Kuznetsova & Connolly 2007](#); [Kunz et al. 2007](#); [Rodney & Tonry 2009](#); [Gong et al. 2010](#); [Falck et al. 2010](#)). In such methods, the lightcurves in different filters for the SN under consideration are compared with those from SNe whose types are well established. Usually, composite templates are constructed for each class, using high signal-to-noise observations of lightcurves of well-studied SNe (see [Nugent et al. 2002](#)), or spectral energy distribution models of SNe. Such methods can produce good results, but the

final classification rates are very sensitive to the characteristics of the templates used. One of the best-known approaches of this type is PSNID (Sako et al. 2008, 2011), which avoids many of the difficulties encountered by simpler methods.

To address the issue of sensitivity to the templates used, Newling et al. (2011) instead fit a parametrised functional form to the SN lightcurves. These post-processed data are then used in either a kernel density estimation method or a “boosting” machine learning algorithm, as discussed by Newling et al. (2011), to assign a probability to each classification output, rather than simply assigning a specific SN type. More recently, Richards et al. (2012) and Ishida & de Souza (2012) have introduced methods for SN photometric classification that do not include on any form of template fitting, but instead employ a mixture of dimensional reduction of the SN data coupled with a machine learning algorithm. Richards et al. (2012) proposed a method that uses a semi-supervised learning approach applied to a database of SNe: first, a low-dimensional representation of each SN is constructed from a simultaneous analysis of all the lightcurves in the database. A classification model is then built in this low-dimensional “feature space” by learning from a set of spectroscopically confirmed training samples. This is subsequently used to estimate the type of each unknown SN.

Subsequently, Ishida & de Souza (2012) proposed the use of Kernel Principal Component Analysis as a tool to find a suitable low-dimensional representation of SN lightcurves. In constructing this representation, only a spectroscopically confirmed sample of SNe is used. Each unlabeled lightcurve is then projected into this space and a k -nearest neighbour algorithm performs the classification.

During my PhD studies, I also developed methods of photometric SNe classification. In Paper III, I introduce an algorithm of SN classification between SN Ia and non-Ia (see Section 6.3) which does not involve templates. In Paper V, I further improve this method by including a HNN technique.

3.3 Searching for SNe

Having discussed the main observational techniques used for SN measurements and giving a brief description how to distinguish between different SN types, I now describe of how SN surveys are undertaken. Modern surveys typically require the following steps in order to observe and classify SNe: (i) finding the events; (ii) identifying the nature of the events using spectroscopic follow-up; (iii) measuring the lightcurve of interesting events in as many bands (see Figure 3.1) as possible.

3.3.1 Finding events

The main technique used to search for SNe is image subtraction. Since SNe are transient events one can subtract search images taken at different times to make non-variable objects disappear. This method was proposed in [Hansen, Jorgensen, & Norgaard-Nielsen \(1987\)](#) and first applied to real observations in [Norgaard-Nielsen et al. \(1989\)](#). By taking images obtained at the rate of about twice or thrice per month, one is very likely to detect SNe at their rising epoch, which is often early enough to trigger spectroscopic and photometric follow-up observations. This type of search greatly benefits from imaging as large a field of view as possible.

Since it is often impossible to have photometric follow-up for all detected objects, one can implement a rolling search method, which consists of repeatedly imaging the same sky patch, and using the image sequence not only for SN detection, but also for measuring their lightcurves. This not only saves on photometric follow-up, but also has the advantage that several SNe might be observed in the same field of view and produces deep images in long-duration surveys. This technique was very successfully implemented in ground-based surveys, see Section [3.3.3](#).

3.3.2 Follow-up observations

Spectroscopic follow-up: As was mentioned previously, spectroscopic follow-up typically requires a telescope of twice the diameter of the one used for imaging. In terms of frequency resolution, since SN spectra do not have narrow lines then $\lambda/\delta\lambda \sim 100$ is sufficient for classification purposes, but $\lambda/\delta\lambda \sim 1000$ is required to measure the redshift sufficiently accurately, which is another important role of spectroscopic follow-up. These observational requirements mean that only a small fraction of SNe will have their spectra measured. Thus, it is common during the image subtraction stage to attempt a pre-classification to identify the most interesting candidates.

The most challenging part of SN spectroscopy is to perform host galaxy subtraction. Since the SNe are point sources, whereas their host galaxies are extended, the fraction of host galaxy light mixed with SN light will increase with redshift. For photometry this problem is solved by making image subtractions, but this solution is infeasible for spectroscopy. One of the current approaches is simply to ignore the problem and make a selection against SNe with bright host galaxies. Another way to address the problem is to use libraries of observed SNe and galaxies to synthesize the observed spectra ([Howell et al. 2005](#)). Finally, an

unavoidable downside of spectroscopy is its “single-mindedness”, owing to the small field of view of most instruments.

Photometric follow-up: In contrast to spectroscopic observations, photometric follow-up does not require large observational facilities. The only constraint is that the images have enough stars to serve as photometric and geometric anchors. Astronomical photometry requires measurements of the source of interest together with some standard stars using the same instrument. With more and more rolling search surveys, photometric follow-up will become increasingly unnecessary, especially with most interest focussing on high- z SNe, but it will still play a major role for searches for nearby SNe.

3.3.3 Surveys

Since the early 1990s, many independent teams have explored the sky for SNe. Some of them have targeted low redshifts, and others have looked as deep as possible with present technologies. And the SN search quest continues . . .

In this section I will describe the major SNIa surveys of the past, present and future, and discuss their main observational techniques, the time of data collection and the number of SNe observed.

History of pioneering SN surveys

The oldest SN survey is the Calan–Tololo survey (Hamuy et al. 1995, 1996), which observed a sample of “nearby” SNe at redshifts below roughly 0.1. Photometry and spectroscopy for these SNe were measured on relatively small telescopes, of 1 m and 2 m in diameter, respectively.

After the great success of Calan–Tololo, in the mid-90s two teams started a search for high- z SNe in order to use them as standard candles: the Supernova Cosmology Project (SCP) and the high- z team (HZT). By 1995 the projects were already yielding their first promising results, and both teams consequently received plenty of observational time, including photometric follow-up with the Hubble Space Telescope (HST). The results from each team were published in Riess et al. (1998) and Perlmutter et al. (1999), with 10 and 42 distant SNe respectively, and they came to the same conclusion: that the expansion of the Universe is accelerating. Such a surprising and profound discovery was obviously a very strong reason to continue the search for further distant SNe.

The accuracy of the colour measurement was, however, a major problem in these works, and so measuring accurate lightcurves was essential in order to improve high- z SN results. From 1997, HST started a new program on photometric follow-up of ground-based searches, followed in 2002 by an independent

Name	ESSENCE	SNLS	SDSS
Imager	CTIO 4-m on the 0.36 deg ² Mosaic-II	CFHT 3.6-m equipped with 1 deg ² Megacam	SDSS 2.5-m with its 1.52 deg ² camera
Bands	R, I	g, r, i, z	u, g, r, i, z
z range	[0.3,0.7]	[0.2,1.0]	[0.1,0.4]
Location	Northern Chile	Hawaii	Apache Point, US
Monitored regions	36 points (i.e. ~ 10 deg ²)	4 points (i.e. ~ 10 deg ²)	300 deg ² equatorial stripe
Frequency	4th night	4th to 5th night	2nd night
Period	for a 3-month per seasons 2003-2008	as long as points remained visible 2003-2008	3 months per year 2005-2007 years
$N_{\text{SN events}}$	~ 100	~ 250	~ 370

Table 3.1: Summary of second generation SN surveys.

program for finding faint high- z events using the Advanced Camera for Surveys (Knop et al. 2003; Riess et al. 2004, 2006). This search allowed the collection of good SN data, with events up to $z \sim 1.0$.

Second generation of SN surveys

Within a decade of the success of Calan–Tololo, a few low- z SN surveys had targeted nearby sky for SNe: CfA (Riess et al. 1999; Jha et al. 2006; Hicken et al. 2009), the Carnegie Supernova Project (CSP; Contreras et al. 2009) and the Lick Observatory Supernovae Search (LOSS; Li et al. 1999), which provides events both inside and outside the Hubble flow. The latest completed nearby SN survey is SNFactory (Copin et al. 2009; Thomas et al. 2009; Bailey et al. 2009). The data from all these nearby searches now provides an excellent low-redshift “anchor” for cosmological studies using high- z SNe.

The second generation of high- z surveys include: ESSENCE (Miknaitis et al. 2007), SNLS (Astier et al. 2005) and SDSS (Holtzman et al. 2008), each of which used the rolling search technique. Their goal was to increase both the number and quality of well-measured high- z SNIa. Indeed, many lightcurves for high- z SNe have been collected, but unfortunately not all detected SNe have spectroscopic follow-up observations and measured redshifts, since using 4-m

and 8-m class telescopes for all of them was not feasible. A summary of these surveys is presented in Table 3.1.

Joint analysis

To place tight constraints on cosmological parameters, one needs a set of SNe at a range of redshifts, with coherent distance estimates and a good understanding of all systematic errors. This is usually achieved by the analysis of SN compilations from different surveys, since covering a large redshift range generally requires different instruments. Any new compilation also typically contains new events and state-of-the-art techniques for photometric calibration, and delivers correlated uncertainties.

The most commonly used compilation is “Union”, which has had a few generations: Union (Kowalski et al. 2008), Union2 (Amanullah et al. 2010) and the latest Union2.1 (Suzuki et al. 2012), and was very successful in making SN data more accessible for cosmological analysis outside of the SN community, where most of the users are primarily interested in cosmology constraints, and not so interested in parameters associated with the SNe themselves. In addition to the “Union” compilation, one should also mention the most recent compilation, published in the latest SDSS data release paper by Betoule et al. (2014). Indeed, the cosmological constraints derived from this latest survey were shown in Figure 1.5 in the Introduction.

One does, however, have to be very careful when combining data-sets together. The joint analysis of combined surveys comes at a price, since one must first check that the individual SN surveys produce results that are mutually consistent. If this is not the case, any results derived from their combination may be misleading. In Paper IV, I present a method to perform this task and apply it to existing compilations.

Current and future SN surveys

The intermediate Palomar Transient Factory (iPTF) is one of the nearby SN surveys currently in operation. Built as a continuation of the Palomar Transient Factory, it has now collected data for about 2200 SNe, out of which about 1400 are SNIa. The observations are made in the R- and g-band and most of them have spectroscopic follow-ups. In 2016, iPTF will be transformed into the Zwicky Transient Factory (ZTF). Using a reworked version of the same telescope as iPTF, ZTF will use a new camera: the world’s largest in field-of-view at nearly 50 deg^2 . This new camera will enable a full scan of the visible sky every night.

CSP II is another nearby SNe search started in 2011 and anticipated to operate for five years. The difference between this survey and iPTF is that, rather than performing optical observations, it collects data in the near infrared and, together with time-series spectroscopy, it tries to achieve a distance precision of 1-2% to build a definitive low-redshift reference for future rest-frame infrared observations of distant SNIa.

The Pan-STARRS (Panoramic Survey Telescope and Rapid Response System) constitutes a new generation of rolling search surveys. Designed in the University of Hawaii's Institute for Astronomy, it has a wide-field camera that can make images of the whole sky every four nights. So far, only 1.5 years of results have been obtained (Rest et al. 2013; Scolnic et al. 2013), which has resulted in 146 spectroscopically confirmed SNIa at $0.03 < z < 0.65$.

Another high- z survey currently in operation is DES, which saw first-light in 2012 and will continue for five years. This survey operates on the Blanco 4-meter telescope in the Chilean Andes, with a 570-Megapixel digital camera, DECam. DES surveys a large swathe of the southern sky and will provide deep images of it. DES plans to obtain well sampled lightcurves for more than several thousand SNe. Unfortunately, DES does not have a spectroscopic follow-up program, and so will have to rely on photometric classification methods to determine which SNe are of Type Ia.

Finally, I would like to mention that the Large Synoptic Survey Telescope will begin operations in 2019 and will photograph the entire available sky every few nights and have data of outstanding quality. If all goes well, science observations will commence in 2021.

Several mission concepts to measure SNe from space have also been developed; unfortunately none of them passed the selection processes. Working from space is crucial at $z \gtrsim 1$, because reliable distances should then be measured in the near infrared, in order to allow a direct comparison with nearby events measured in blue bands.

3.4 SNIa

Since SNIa are those used in cosmology, they have become the most studied type of SNe. In this Section, I briefly describe the physics of SNIa explosions and ways in which they can be standardised for use in cosmology.

3.4.1 Explosion models

The physics of a SNIa explosion, one of the most energetic events in the Universe, is still unclear. The most popular hypothesis is that the SNIa is a thermonuclear explosion in carbon–oxygen white dwarfs in close binaries (Hoyle & Fowler 1960; Nomoto, Iwamoto, & Kishimoto 1997). Thielemann et al. (2004) show that the observed amount of energy in SNIa explosions is approximately the amount of energy that would be produced in the conversion of carbon and oxygen into iron. In order for this process to occur, white dwarfs must be close to the Chandrasekhar mass, so that carbon ignition can start. A realistic way for a white dwarf to grow to the Chandrasekhar mass is through mass transfer within a close binary. Unfortunately, the nature of the stars that can be the donors is not clear. Also, no progenitor system before a SN explosion has been conclusively identified. Another problem with this model is that there is observational evidence for systems where the progenitor has a mass much lower (e.g. Foley et al. 2009) or higher (e.g. Howell et al. 2006) than the standard Chandrasekhar mass. Leading models for the SNIa progenitor are single-degenerate (Whelan & Iben 1973; Nomoto 1982) and double-degenerate (Tutukov & Yungelson 1981; Iben & Tutukov 1984; Webbink 1984). There are many good reviews of this topic, see e.g. Wang & Han (2012); Hillebrandt & Niemeyer (2000).

The nature of SNIa explosions is interesting not only from the point of view of stellar and galaxy evolution, but also for cosmological studies. Early studies of nearby SNe and numerical simulations of their explosion models have been used to derive the value of H_0 (Branch 1992; Hoeflich & Khokhlov 1996; Stritzinger & Leibundgut 2004). Unfortunately, this is the only example when explosion models have been used to infer cosmological parameters. The reason for this is the complexity of the explosion and the consequent light production. SN lightcurve models discussed in Section 3.4.3 can only broadly reproduce observed lightcurves. The same holds for the models of spectra. Improving the models could allow us to use them as templates for fitting data, which would reduce the distance scatter, and give insights into redshift-dependent systematic biases in distances.

3.4.2 SN lightcurves

A SNIa emits most of its energy in the visible light, with some energy in the near UV and near IR. As was noted early on, SNIa have reproducible lightcurves (Minkowski 1964), as shown in the left panel of Figure 3.3, but with very different behaviour in different colours; the example of SN2006D is shown in the right panel of Figure 3.3.

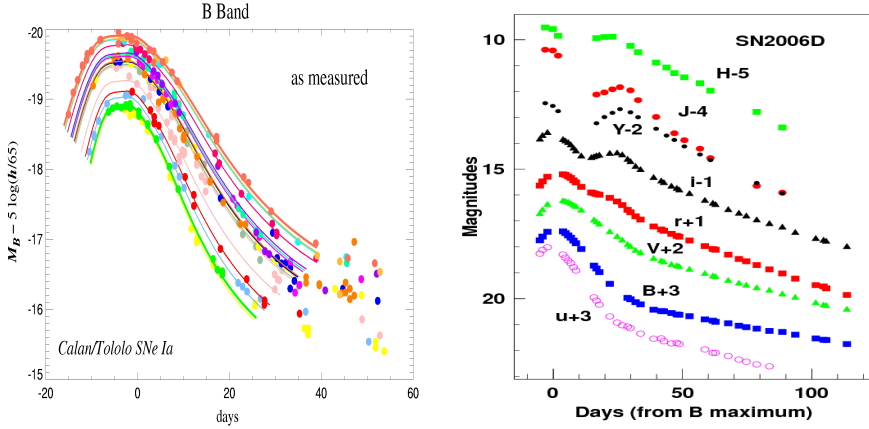


Figure 3.3: Left panel: SN lightcurves in the B-band. Credit: Perlmutter (2003). Right panel: Lightcurves in different bands. Credit: [Astier \(2012\)](#).

In the left panel of Figure 3.3 one can see that SNIa exhibit a variability in the width of their lightcurves. Accounting for time dilation in order to compare restframe widths does not completely eliminate this difficulty. The problem was “solved” in 1993 from a small sample of well-measured events ([Phillips 1993](#)). The Phillips relation quantifies how SNe that are intrinsically brighter have lightcurves that decline more slowly from their maximum. This relation is central to the use of SNIa for measuring cosmological distances. Moreover, in the *B*-band, this variability of lightcurves is typically described by stretching the time axis of a single lightcurve template ([Perlmutter et al. 1997](#); [Goldhaber et al. 2001](#)). The rise and fall timescales seem to vary together for [Goldhaber et al. \(2001\)](#) and [Conley et al. \(2006\)](#), while [Hayden et al. \(2010\)](#) finds them to be essentially independent.

SNIa also exhibit variability in their colours (measured, e.g. at maximum) even at a fixed decline rate ([Guy et al. 2010](#); [Blondin et al. 2009](#)). The source of colour variability, which is unrelated to the decline rate, is still unclear. One of the options is that SNe intrinsically have different colors (e.g. [Foley & Kasen 2011](#)), while another hypothesis relates it to extinction by dust in the host galaxy. Most likely the truth is a mixture of both and possibly some other astronomical reasons that we do not yet understand.

To use SNIa for cosmological searches, their fluxes must be expressed in the same way, and for this purposes one uses lightcurve fitters.

3.4.3 Standardization of SNe

Using empirical lightcurve models not only “standardises” SN lightcurves, but also “compresses” the photometric data characterizing an event. The aim of all the lightcurve models can be summarised as the derivation of a distance, for which one needs a brightness (anything that scales linearly with the observed flux), the decline rate and colour.

In the original work of Phillips (1993), the data measurements were very well sampled, so there was no need for an explicit model. Phillips built smooth discrete templates with different Δm_{15} values, where this quantity denotes the decline rate measured as the magnitude difference between peak and 15 (rest-frame) days later. Hamuy et al. (1995) generalised this method to allow it to fit much more sparse observations. This method enjoyed broad usage and the resulting templates have been continuously updated (Phillips et al. 1999; Germany et al. 2004; Prieto, Rest, & Suntzeff 2006). Recently, the SNOOPY model (Burns et al. 2011) revisited the Δm_{15} paradigm with an extension of it into the near IR. Another method was used to account for the decline-rate variation: the “stretch” paradigm (Perlmutter et al. 1997) proposed to stretch the time axis of these templates in the B and V bands. A disadvantage of all these types of models is that they rely on lightcurve templates.

Spectral Adaptive Lightcurve Template 2 (SALT2)

The most commonly used empirical lightcurve model is currently SALT2 (Guy et al. 2007; Mosher et al. 2014). The main idea behind this method is that all the measurements are fit using a function of the phase p and the wavelength λ

$$F(p, \lambda) = x_0 [M_0(p, \lambda) + x_1 M_1(p, \lambda)] \exp[c \text{ CL}(\lambda)], \quad (3.1)$$

where M_0 is the mean SNIa spectral energy distribution, M_1 accounts for lightcurve width variations, CL is a color law which incorporates any wavelength-dependent color variations and is independent of epoch, x_1 is the lightcurve shape parameter, x_0 is the overall flux scale and c is the peak B–V color. The first three of the above parameters are SN-independent and describe all SNIa, whereas the last three parameters are unique for each SN. No assumptions about dust or extinction laws are made a priori. A cartoon schematic of the SALT2 training process is shown in Figure 3.4.

SALT2 also allows one to accommodate the intrinsic variability of SNIa. To achieve this, the model includes sources of additional uncertainty. These are a broadband magnitude scatter $k(\lambda)$, which deals with the color law and the c parameter, and a spectral “error snake” $S(p, \lambda)$ to account for the x_1 parameter.

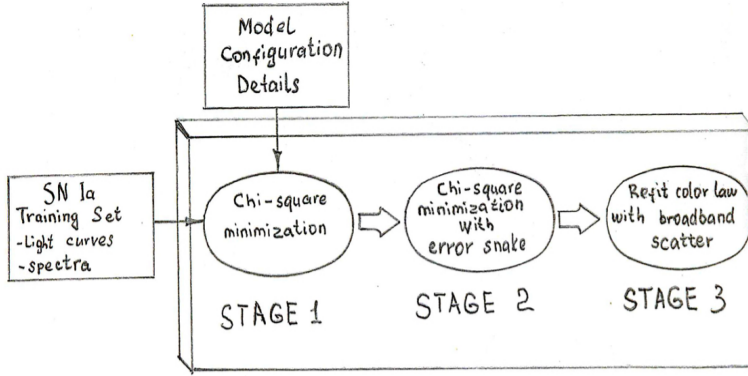


Figure 3.4: The three stages of the SALT2 model training process. Each stage calculates best-fit model parameters using successively improved estimates of model uncertainties.

In order to calculate and include these effects, SALT2 performs three iterations of χ^2 -minimisation, as illustrated in Figure 3.4.

As a result, for each SN, SALT2 reports best-fit values $\hat{x}_0, \hat{x}_1, \hat{c}$, the redshift \hat{z} , and the covariance matrix

$$\hat{C}_{\text{SALT2}} = \begin{pmatrix} \sigma_{x_0}^2 & \sigma_{x_0, x_1} & \sigma_{x_0, c} \\ \sigma_{x_0, x_1} & \sigma_{x_1}^2 & \sigma_{x_1, c} \\ \sigma_{x_0, c} & \sigma_{x_1, c} & \sigma_c^2 \end{pmatrix}. \quad (3.2)$$

Let us denote the result of the SALT2 lightcurve fitting procedure as

$$D_{\text{SALT2}, i} = \{\hat{z}_i, \hat{x}_{0i}, \hat{x}_{1i}, \hat{c}_i, \hat{C}_{i, \text{SALT2}}\}, \quad (3.3)$$

where i runs through the n SNe in the sample. These outputs can be used to obtain distance estimates for the SNe using Eq. 4.5.

Other lightcurve models and distance estimators

As mentioned previously, the SALT2 model is one of the most frequently used SN lightcurve fitters. Together with SALT (Guy et al. 2005; Astier et al. 2006) and SiFTO (Conley et al. 2008), it mostly uses the “stretch” paradigm. SALT is just a earlier version of SALT2, whereas SiFTO models the lightcurves from

spectral energy distribution templates. SiFTO uses the fact that SN lightcurves have different shapes in different bands (see the right panel of Figure 3.3). As in SALT2, these methods do not give direct distant estimates, but one needs to use equations of the form of Eq. 4.5. One can also perform analyses with combined SALT2/SiFTO fits, see e.g. [Guy et al. \(2010\)](#).

Another frequently used model is the Multi Light Curve Shape (MLCS, [Riess, Press, & Kirshner 1996](#)) model, which consists of a one-parameter family of lightcurve shapes with standard visible bands B, V, R and I, see Figure 3.1. This complete model of SN lightcurves depends on three parameters (plus a reference date): a distance modulus, a brightness offset, and an extinction value. Initially trained on 12 events it was updated to about 100 events. Also, the model has been extended towards the blue by adding the U-band. This second version is named MLCS2k2 ([Jha, Riess, & Kirshner 2007](#)).

Among other methods are the Bayesian Adapted Template Match method ([Tonry et al. 2003](#)), the so-called “Bailey ratio” ([Bailey et al. 2009](#)), the CMagic distance estimator ([Wang et al. 2003](#)), the Gaussian-process regression method ([Kim et al. 2013](#)), plus many more.

Unfortunately, not only is none of these methods the “correct” one, but the cosmological parameter constraints one obtains using the same data but different lightcurve fitting methods are significantly different. Comparisons between SALT2 and MLCS2k2 were made in [Kessler et al. \(2009\)](#), which finds that when the restframe *U*-band is taken into account, systematically different distances are obtained. In [Guy et al. \(2010\)](#), SALT2 and SiFTO are compared and the differences obtained are acceptable if the compilation contains the level of a few hundred events.

3.5 Type non-Ia SNe in cosmological analyses

Usually non-Ia SNe are an unwanted contaminant in SNIa compilations. Nevertheless, there is one type of non-Ia SNe that can be used for cosmological analyses. Type II Plateau SNe (SNII-P) can be used as standard candles to determine luminosity distances, although only for smaller distances and with lower accuracy than those of SNIa. Despite this shortcoming, SNII-P explosions are better understood than SNIa. Another advantage of SNII-P is that they have been found only in late-type galaxies, whereas SNe Ia have been observed both in late- and early-type galaxies. Consequently, one would expect distance estimates from SNII-P to suffer less from biases resulting from different galactic environments. This difference in systematic effects allows SNII-P data to complement SNIa analyses ([D’Andrea et al. 2010](#)).

Chapter 4

Cosmological parameter inference using SNe

‘All my Bayesian friends have objected at this point that there’s no such concept as bias in Bayesian analysis. It is true that there is no meaningful, exact definition of bias except in a frequentist sense. What I mean here is that the answer [...] is usually wrong, and in a given direction. The dictionary calls this “bias”.’

Stephen Gull

Undoubtedly the greatest accomplishment of SN studies over the past 20 years is the discovery of the current accelerating expansion of the Universe. This was recognised by the award of the Nobel Prize in Physics in 2011, which was divided one-half to Saul Perlmutter, the other half jointly to Brian P. Schmidt and Adam G. Riess.

In order to constrain cosmological parameters, one needs to make an inference from the observational measurements. It is usual to adopt a two-stage approach in which SN observations are first analysed using a lightcurve fitting program, the outputs of which are then used in a second-stage of inference for the cosmological parameters. The first step of this process was already described in Section 3.4.3. In this chapter, I outline the commonly-used methods of cosmological inference, assessing their advantages and disadvantages. Since the

SALT2 algorithm is the most widely used for SN fitting and I made use of it in my papers, I will also use it here. However, the results and conclusions presented in this Chapter are not specific to SALT2 and can be easily generalised to the outputs of other lightcurve fitting codes like SiFTO, MLCS2k2, etc.

4.1 Comparing theory and observations

As discussed in Section 3.4.3, on the observational side, for each SN, the SALT2 algorithm reports best-fit values \hat{m}_B^* , \hat{x}_0 , \hat{x}_1 , \hat{c} , the redshift \hat{z} , and the covariance matrix \hat{C}_{SALT2} defined in Eq. 3.2. This covariance matrix does not include covariances involving \hat{m}_B^* . We use

$$\sigma_{m_B^*, x_1} = -\frac{5\sigma_{x_0, x_1}}{2x_0 \ln 10} \quad (4.1)$$

$$\sigma_{m_B^*, c} = -\frac{5\sigma_{x_0, c}}{2x_0 \ln 10} \quad (4.2)$$

to construct the covariance matrix

$$\hat{C} = \begin{pmatrix} \sigma_{m_B^*}^2 & \sigma_{m_B^*, x_1} & \sigma_{m_B^*, c} \\ \sigma_{m_B^*, x_1} & \sigma_{x_1}^2 & \sigma_{x_1, c} \\ \sigma_{m_B^*, c} & \sigma_{x_1, c} & \sigma_c^2 \end{pmatrix}. \quad (4.3)$$

Let us denote the result of the SALT2 lightcurve fitting procedure, with the above rescaled covariance matrix, as

$$D_i = \{\hat{z}_i, \hat{m}_{B,i}^*, \hat{x}_{1,i}, \hat{c}_i, \hat{C}_i\}, \quad (4.4)$$

where i runs through the n SNe in the sample.

The data D_i define the “observed” distance modulus μ_i^{obs} for the i th SN as

$$\mu_i^{\text{obs}}(\alpha, \beta, M_0) = \hat{m}_{B,i}^* - M_0 + \alpha \hat{x}_{1,i} - \beta \hat{c}_i. \quad (4.5)$$

This expression contains three unknown parameters, all of which are assumed global, i.e. having the same value for all SNIa. These parameters are: M_0 , the B -band absolute magnitude of the SN, and α , β , which are nuisance parameters controlling the stretch and colour corrections.

On the theory side, in a Friedman-Robertson-Walker cosmology, if an object has an absolute luminosity L and one measures its flux to be F , then its luminosity distance is given by¹

$$D_L \equiv \left(\frac{L}{4\pi F} \right)^{1/2}. \quad (4.6)$$

The distance modulus is defined by $\mu = m - M_0$, where $m \equiv -2.5 \log_{10} F$ is the apparent magnitude of the object and M_0 is its absolute magnitude. Hence, μ can be written as

$$\mu = 5 \log_{10} \left(\frac{D_L}{\text{Mpc}} \right) + 25, \quad (4.7)$$

where the constant offset is included such that one satisfies the convention that $\mu = 0$ at $D_L = 10$ pc.

In terms of the cosmological parameters $\mathcal{C} = \{\Omega_{\text{m},0}, \Omega_{\text{de},0}, H_0, w\}$, an object at a redshift z has the luminosity distance

$$D_L(z, \mathcal{C}) = \frac{c}{H_0} \frac{(1+z)}{\sqrt{|\Omega_{k,0}|}} S \left(\sqrt{|\Omega_{k,0}|} I(z) \right), \quad (4.8)$$

where

$$I(z) \equiv \int_0^z \frac{d\bar{z}}{\sqrt{(1+\bar{z})^3 \Omega_{\text{m},0} + (1+\bar{z})^{3(1+w)} \Omega_{\text{de},0} + (1+\bar{z})^2 \Omega_{k,0}}}, \quad (4.9)$$

in which (neglecting the present-day energy density in radiation) $\Omega_{k,0} \equiv 1 - \Omega_{\text{m},0} - \Omega_{\text{de},0}$ and $S(x) = x$, $\sin x$ or $\sinh x$ for a spatially-flat ($\Omega_{k,0} = 0$), closed ($\Omega_{k,0} < 0$) or open ($\Omega_{k,0} > 0$) universe, respectively. A cosmological constant corresponds to the special case in which the dark-energy equation-of-state parameter has the value $w = -1$ in this case, the present-day density parameter is usually denoted by $\Omega_{\Lambda,0}$.

To compare the observations and theory, one could therefore identify a set of objects ($i = 1, 2, \dots, N$) whose absolute magnitudes are known *a priori* (standard candles), measure their distance moduli and redshifts, and consider the differences (often termed Hubble diagram residuals)

$$\Delta\mu_i = \mu_i^{\text{obs}}(\alpha, \beta, M_0) - \mu(z_i, \mathcal{C}). \quad (4.10)$$

These could then be used to place constraints on the cosmological parameters \mathcal{C} , plus other parameters of interest, such as α, β and M_0 .

¹For simplicity, I refer here to bolometric quantities, i.e. integrated over all frequencies, rather than in terms of fluxes in specific frequency bands.

Parameter	Value used for simulations
σ_{int}	0.01
α	0.12
β	3.2
M_0	-19.3
σ_{m_b}	0.05
σ_{x_1}	0.5
σ_c	0.05
σ_z	0.0001
$\Omega_{\text{m},0}$	0.3
h	0.7

Table 4.1: Parameter values used in the generation of simulated SNIa data, assuming a spatially-flat universe.

One should note, however, that if the standard candles all have the same absolute magnitude M_0 , but this value is unknown, then it is degenerate with the Hubble constant H_0 , as evident from Eqs. 4.6 and 4.8. Perhaps more importantly, Nature has neglected even to provide such a set of “uncalibrated” standard candles. Instead, we must make do with SNIa for which the absolute magnitudes vary, but can nonetheless be standardised, as discussed in Section 3.4.

4.2 Toy simulations of SN data

In order to discuss the advantages and disadvantages of different inference methods, I apply them to toy simulated SNIa data. In these simulations I assume that the off-diagonal elements of the covariance matrix in Eq. 4.3 are zero; this makes a negligible difference since the off-diagonal elements are very small in practice.

To make the simulation, the procedure below is performed for each SN ($i = 1, 2, \dots, N_{\text{SN}}$), and the values of the various parameters used in the simulations are given in Table 4.1.

1. The redshift is drawn independently from $z_i \sim U(0, 1)$, where $U(a, b)$ denotes a uniform distribution in the range $[a, b]$.
2. The predicted $\mu_i(z_i, \mathcal{C})$ is calculated using Eq. 4.7.

3. The hidden variables M_i , $x_{1,i}$ and c_i are drawn from the respective distributions $M_i \sim \mathcal{N}(M_0, \sigma_{\text{int}}^2)$, $x_{1,i} \sim U(-5.0, 3.0)$ and $c_i \sim U(-0.2, 0.3)$, where $\mathcal{N}(\mu, \sigma^2)$ denotes a normal (Gaussian) distribution with mean μ and variance σ^2 .
4. The value of $m_{B,i}^*$ is calculated using the Phillips relation $m_{B,i}^* = \mu(z_i, \mathcal{C}) + M_i - \alpha x_{1,i} + \beta c_i$.
5. The simulated observational data are obtained by drawing independently from the distributions $\hat{z}_i \sim \mathcal{N}(z_i, \sigma_{z,i}^2)$, $\hat{m}_{B,i}^* \sim \mathcal{N}(m_{B,i}^*, \sigma_{m_{B,i}^*}^2)$, $\hat{x}_{1,i} \sim \mathcal{N}(x_{1,i}, \sigma_{x_{1,i}}^2)$ and $\hat{c}_i \sim \mathcal{N}(c_i, \sigma_{c,i}^2)$.

For my simulations, I generated 100 independent data-sets, each one containing 200 SNe. In my analyses, I assume $h = 0.7$ (as is established to a few per cent accuracy by a number of cosmological probes) and vary $\Omega_{\text{m},0}$, M_0 , α and β .

4.3 Naive definition of the likelihood

Assuming that the Hubble diagram residuals are Gaussian-distributed one often defines the likelihood as

$$\mathcal{L} = \prod_{i=1}^{N_{\text{SN}}} \frac{1}{\sqrt{2\pi}\sigma_i(\alpha, \beta, \sigma_{\text{int}})} \exp \left\{ -\frac{[\mu_i^{\text{obs}}(\alpha, \beta, M_0) - \mu_i(\mathcal{C})]^2}{2\sigma_i^2(\alpha, \beta, \sigma_{\text{int}})} \right\}. \quad (4.11)$$

In this expression, I have included the dependence on (only) the parameters to be fitted. Here the total dispersion σ_i^2 is given by:

$$\sigma_i^2 = (\sigma_{\mu,i}^z)^2 + \sigma_{\text{int}}^2 + \sigma_{\text{fit},i}^2(\alpha, \beta). \quad (4.12)$$

The three components arise as follows:

1. Uncertainties in the peculiar velocity and/or the spectroscopic measurements of either the host galaxy or SNIa itself lead to an uncertainty $\sigma_{z,i}$ in its estimated redshift, which in turn induces an error $\sigma_{\mu,i}^z$ in the distance modulus.
2. Even after correction for stretch and colour, there remains some global variation in the SNIa absolute magnitudes. The quantity σ_{int} contains all of these intrinsic dispersion errors.

3. The uncertainty in the fitting of the parameters by SALT2 is given by

$$\sigma_{\text{fit},i}^2 = \psi^t \hat{C}_i \psi, \quad (4.13)$$

where the transposed vector $\psi^t = (1, \alpha, -\beta)$ and \hat{C}_i is the covariance matrix given in Eq. 4.3.

Additional errors, such as those due to lensing or Milky Way dust extinction can also be added in at this stage, but I do not consider such errors here.

For convenience, one often writes Eq. 4.11 in the form:

$$-\ln(L) = \text{const} + \sum_{i=1}^{N_{\text{SN}}} \frac{[\mu_i^{\text{obs}} - \mu_i]^2}{2\sigma_i^2} + \sum_{i=1}^{N_{\text{SN}}} \ln(\sigma_i). \quad (4.14)$$

As shown in Figure 4.1, maximising this function unfortunately leads to biased results for some of the parameters. This is particularly acute for the β parameter. This effect stops us using the likelihood in Eq. 4.11, although it has been employed and investigated in some previous analyses (D’Agostini 2005).

It is worth pointing out that, in the case when the error bars on the color and stretch parameters are small, the biases “disappear”, as one can see in Figure 4.2.

Gull (1989) identified the origin of the problem, albeit in the conceptually more straightforward context of fitting a straight line

$$y = ax + b, \quad (4.15)$$

to a set of data (x_i, y_i) where the x_i and y_i both have an associated measurement error and a, b are the parameters of the model. One can see that this linear toy model is very similar to the relation between the parameters in Eq. 4.5, where the parameters a, b of the linear model correspond to the parameters α, β . I will return to Gull’s findings in Section 4.5, but I first describe the more pragmatic, empirical approach adopted by the SN community to address the problem of bias associated with the use of Eq. 4.5.

4.4 The standard χ^2 -method

The precise methods used for the estimation of cosmological parameters differ between SN consortia, but the main elements are common to all. Central to the approach is the χ^2 -statistic, which is defined as

$$\chi^2(\mathcal{C}, \alpha, \beta, M_0, \sigma_{\text{int}}) = \sum_{i=1}^{N_{\text{SN}}} \frac{[\mu_i^{\text{obs}}(\alpha, \beta, M_0) - \mu_i(\mathcal{C})]^2}{\sigma_i^2(\alpha, \beta, \sigma_{\text{int}})}, \quad (4.16)$$

where σ_i^2 is that given in Eq. 4.12.

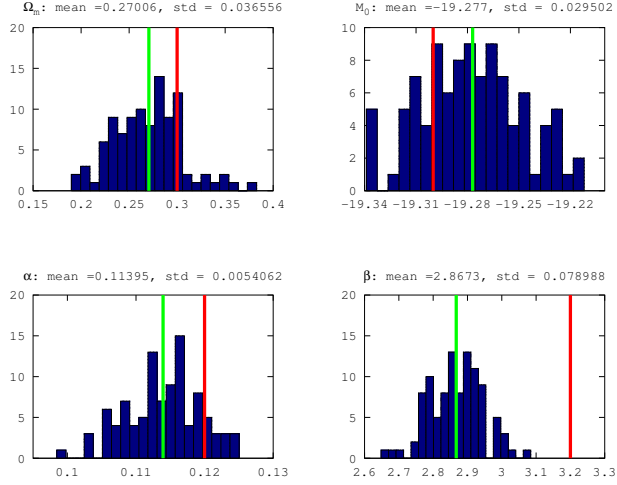


Figure 4.1: Histograms showing the distribution of the point estimates of the parameters $\Omega_{m,0}$, M_0 , α and β . The green vertical lines show the mean values of the point estimates, and the solid red vertical lines show the true values of the parameters used to simulate the data. The data are analysed using the naive likelihood method.

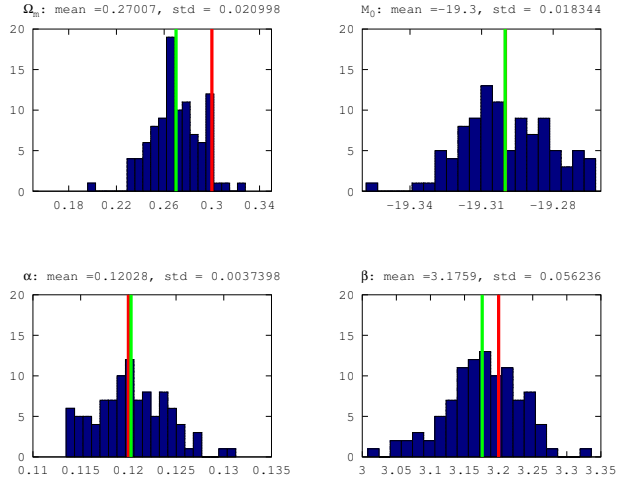


Figure 4.2: The same as Figure 4.1, but for simulations generated using the values $\sigma_{x_1} = 0.1$ and $\sigma_c = 0.01$.

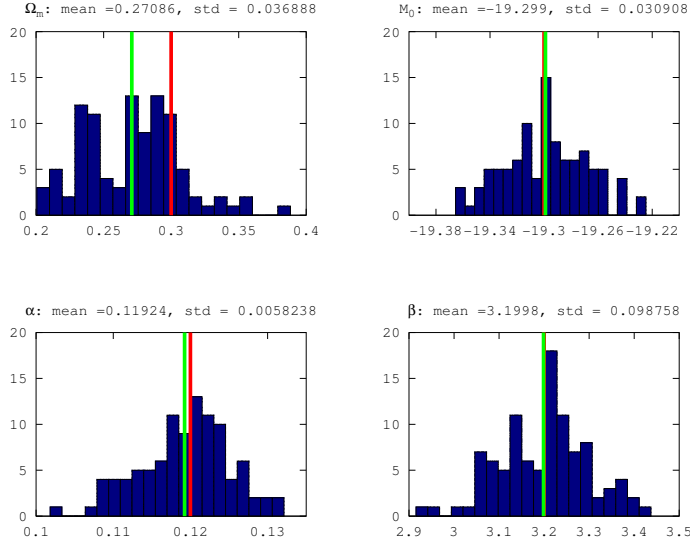


Figure 4.3: The same as Figure 4.1, but for simulations analysed with the χ^2 -method.

We see that this expression is merely the second term on the right-hand side of Eq. 4.14. The full expression for the (minus) log-likelihood on the right-hand side of Eq. 4.14 contains two competing terms: minimisation of the second term (χ^2) would favor large values of σ_i , whereas minimisation of the third term would favor small values of σ_i . In Eq. 4.16 this last term is simply ignored. Somewhat surprisingly, it has been established through simulation that discarding this term removes the bias in the estimated parameters, provided σ_{int} is held fixed. It is fair to say that the fundamental reason for this “magical” removal of the bias is not well understood, even by those members of the SN community that use the method on a regular basis.

Typically, the χ^2 -function (Eq. 4.16) is minimized simultaneously with respect to the cosmological parameters \mathcal{C} and the global SNIa nuisance parameters α , β and M_0 . This minimisation can, however, be performed using different search algorithms (e.g. MCMC techniques or grid searches) and the treatment of M_0 (which is degenerate with H_0), in particular whether this parameter is marginalised over analytically or numerically.

There remains, however, the issue of determining an appropriate value for σ_{int} , which is usually performed as follows. Once the minimum value of χ^2 has been obtained, the value of σ_{int} is estimated by requiring that $\chi^2_{\text{min}}/N_{\text{dof}} \sim 1$; this process is usually iterated until convergence is obtained.

The χ^2 -method has been fully tested and proven to be satisfactory for cosmological parameter inference. Results from the toy example are shown in Figure 4.3. Nevertheless, the method does have a few problems:

1. The use of χ^2 in Eq. 4.16 is not statistically well-motivated, but is based only on empirical evidence and experience (Gull 1989).
2. The global parameters α, β appear in both the numerator and denominator, since they act as both range and location parameters. Thus, the errors on α, β are not Gaussian. The informal test which states that $\chi_{\min}^2/N_{\text{dof}} \sim 1$ for a good fit model only holds in the Gaussian case. Hence its use cannot be justified here.
3. Since I use an unnormalised likelihood (without the second term on the right-hand side of Eq. 4.14), one can not calculate the Bayesian evidence, and hence model selection is not possible. One can look on this problem differently: every model will fit the data equally well, since by construction σ_{int} is determined by demanding that $\chi_{\min}^2/N_{\text{dof}} \sim 1$.
4. This method obtains only a best value for σ_{int} without any indication of the error on that value.

4.5 BHM

Gull (1989) solved the problem of fitting a straight line to data with errors in both x and y . The abstract of this paper is reproduced below:

‘A Bayesian solution is presented to the problem of straight-line fitting when both variables x and y are subject to error. The solution, which is fully symmetric with respect to x and y , contains a very surprising feature: it requires an informative prior for the distribution of sample positions. An uninformative prior leads to a bias in the estimated slope.’

In essence, this bias is the same as that which stopped us from using the likelihood in Eq. 4.11 for estimating cosmological parameters.

Gull’s proposed solution has two main steps:

1. Introduction of “hidden variables”, which are the “true” values of the measured quantities; these variables are nuisance parameters and will be integrated away in the end.

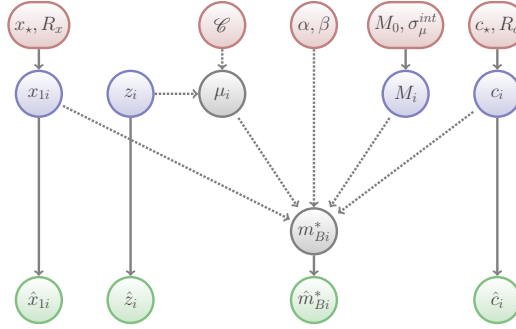


Figure 4.4: Graphical network showing the deterministic (dashed) and probabilistic (solid) connections between variables in the BHM. Variables of interest are in red, hidden (unobserved) variables are in blue and observed data (denoted by hats) are in green. Credit: [March et al. \(2011a\)](#).

2. The imposition of an informative prior on these variables, which contains hyper-parameters that are allowed to vary simultaneously with the other parameters, and are then marginalised over.

These ideas were implemented in the context of SN cosmological analyses in the BHM ([March et al. 2011a](#)).

In this method one considers a probability for the full catalogue of SNe *simultaneously*, since the form of the BHM likelihood for a set of SN observations ($i = 1, 2, \dots, N$) is *not* simply the product of the likelihoods for each individual SN.

One begins by considering the probability

$$P \equiv \Pr(\hat{\mathbf{m}}_B^*, \hat{\mathbf{x}}_1, \hat{\mathbf{c}}, \hat{\mathbf{z}}, \mathbf{m}_B^*, \mathbf{x}_1, \mathbf{c}, \mathbf{z}, \mathbf{M} | \mathcal{C}, \alpha, \beta, \sigma_{\text{int}}, \hat{\mathbf{C}}, \sigma_z), \quad (4.17)$$

where boldface symbols denote vectors containing the corresponding parameters for each SN ($i = 1, 2, \dots, N$). I denote the parameters of the model to be fitted by $\phi = \{\mathcal{C}, \alpha, \beta, \sigma_{\text{int}}\}$, and those assumed known by $\psi = \{\hat{\mathbf{C}}, \sigma_z\}$.

The BHM likelihood function described in [March et al. \(2011a\)](#) is obtained by marginalising Eq. 4.17 over the hidden variables, together with other nuisance parameters describing the SN population. One can see the relation between different types of variables in this model in Figure 4.4. Thus, one obtains $\mathcal{L}_{\text{BHM}}(\phi) \equiv \Pr(\hat{\mathbf{m}}_B^*, \hat{\mathbf{x}}_1, \hat{\mathbf{c}}, \hat{\mathbf{z}} | \phi, \psi)$ by marginalising as follows:

$$\mathcal{L}_{\text{BHM}}(\phi) = \int \cdots \int d\mathbf{m}_B^* d\mathbf{x}_1 d\mathbf{c} d\mathbf{z} d\mathbf{M} \Pr(\hat{\mathbf{m}}_B^*, \hat{\mathbf{x}}_1, \hat{\mathbf{c}}, \hat{\mathbf{z}}, \mathbf{m}_B^*, \mathbf{x}_1, \mathbf{c}, \mathbf{z}, \mathbf{M} | \phi, \psi). \quad (4.18)$$

To perform this marginalisation, one assumes that: (i) the measured redshift \hat{z}_i is independent of $\hat{m}_{B,i}^*$, $\hat{x}_{1,i}$ and \hat{c}_i ; (ii) the true redshift z_i is independent of M_i , x_i , c_i , and (iii) the exact relationship $\mu(z_i, \mathcal{C}) = m_{B,i}^* - M_i + \alpha x_{1,i} - \beta c_i$ between the hidden variables holds. This enables one to write Eq. 4.17 as

$$P = \Pr(\hat{\mathbf{m}}_B^*, \hat{\mathbf{x}}_1, \hat{\mathbf{c}} | \mathbf{m}_B^*, \mathbf{x}_1, \mathbf{c}, \hat{\mathbf{C}}) \Pr(\hat{\mathbf{z}} | \mathbf{z}, \boldsymbol{\sigma}_z) \Pr(\mathbf{M}, \mathbf{x}_1, \mathbf{c} | \sigma_{\text{int}}) \Pr(\mathbf{z}) \delta[\mathbf{m}_B^* - \mathbf{M} + \alpha \mathbf{x}_1 - \beta \mathbf{c} - \mu(\mathbf{z}, \mathcal{C})]. \quad (4.19)$$

The presence of the delta-function allows one to perform the integral over \mathbf{m}_B^* immediately. Moreover, the first two probability distributions on the right-hand side are simply the product of the corresponding distributions for each SN separately, namely

$$\Pr(\hat{\mathbf{m}}_B^*, \hat{\mathbf{x}}_1, \hat{\mathbf{c}} | \mathbf{m}_B^*, \mathbf{x}_1, \mathbf{c}, \hat{\mathbf{C}}) = \prod_{i=1}^N \frac{\exp \left[-\frac{1}{2} (\hat{\mathbf{v}} - \mathbf{v})^t \hat{\mathbf{C}}_i^{-1} (\hat{\mathbf{v}} - \mathbf{v}) \right]}{|2\pi \hat{\mathbf{C}}_i|^{1/2}}, \quad (4.20)$$

$$\Pr(\hat{\mathbf{z}} | \mathbf{z}, \boldsymbol{\sigma}_z) = \prod_{i=1}^N \frac{\exp \left[-(\hat{z}_i - z_i)^2 / (2\sigma_{z,i}^2) \right]}{(2\pi\sigma_{z,i}^2)^{1/2}}, \quad (4.21)$$

where the vector \mathbf{v} is defined by $\mathbf{v} = (\mathbf{m}_B^*, \mathbf{x}_1, \mathbf{c})^t$ and similarly for $\hat{\mathbf{v}}$.

A key difference between the BHM and the standard χ^2 -method is the specification of the prior $\Pr(\mathbf{M}, \mathbf{x}_1, \mathbf{c} | \sigma_{\text{int}})$ on the right-hand side of Eq. 4.19. A common choice is to consider the SNe as true standard candles by assigning $\Pr(M_i) = \delta(M_i - M_0)$, while adopting a uniform normalised top hat distribution on each remaining hidden variable c_i and $x_{1,i}$ (D'Agostini 2005), but this just leads to the naive likelihood discussed in Section 4.3, with σ_{int} set to zero. I therefore impose a different prior here. It is again assumed separable in the sense that $\Pr(\mathbf{M}, \mathbf{x}_1, \mathbf{c} | \sigma_{\text{int}}) = \Pr(\mathbf{M} | \sigma_{\text{int}}) \Pr(\mathbf{x}_1) \Pr(\mathbf{c})$, but each of the distributions on the right-hand side does not factorise into terms corresponding to individual SNe. This occurs since the BHM introduces and marginalises over additional nuisance hyper-parameters M_0 , x_* , R_x , c_* and R_c associated with the

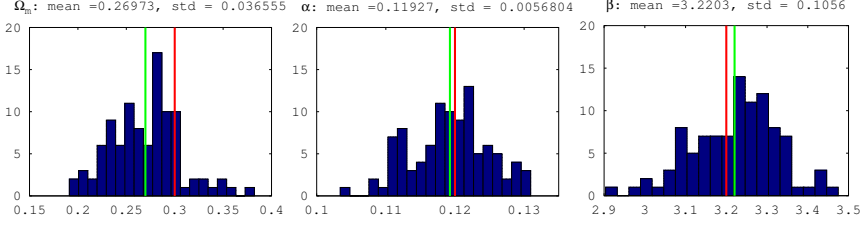


Figure 4.5: The same as Figure 4.1, but for simulations analysed with the BHM. Note that the parameter M_0 is marginalised over analytically.

SN population, and described below. In particular, one writes

$$\Pr(\mathbf{M}|\sigma_{\text{int}}) = \int dM_0 \Pr(M_0) \prod_{i=1}^N \Pr(M_i|M_0, \sigma_{\text{int}}), \quad (4.22)$$

$$\Pr(\mathbf{x}_1) = \iint dx_* dR_x \Pr(x_*) \Pr(R_x) \prod_{i=1}^N \Pr(x_{1,i}|x_*, R_x), \quad (4.23)$$

$$\Pr(\mathbf{c}) = \iint dc_* dR_c \Pr(c_*) \Pr(R_c) \prod_{i=1}^N \Pr(c_i|c_*, R_c), \quad (4.24)$$

in which it is assumed that a number of probability distributions are separable. The prior distribution of each of the hidden variables M_i , $x_{1,i}$, c_i , is assumed to be Gaussian, so that

$$\Pr(M_i|M_0, \sigma_{\text{int}}) = \mathcal{N}(M_0, \sigma_{\text{int}}^2), \quad (4.25)$$

$$\Pr(x_{1,i}|x_*, R_x) = \mathcal{N}(x_*, R_x^2), \quad (4.26)$$

$$\Pr(c_i|c_*, R_c) = \mathcal{N}(c_*, R_c^2). \quad (4.27)$$

Finally, one must also assign the priors on the nuisance hyper-parameters M_0 , x_* , R_x , c_* , R_c , which are taken to be

$$\Pr(M_0) = \mathcal{N}(\bar{M}_0, \sigma_{M_0}^2), \quad (4.28)$$

$$\Pr(x_*) = \mathcal{N}(0, \sigma_{x_*}^2), \quad (4.29)$$

$$\Pr(c_*) = \mathcal{N}(0, \sigma_{c_*}^2), \quad (4.30)$$

$$\Pr(R_x) = 1/R_x, \quad (4.31)$$

$$\Pr(R_c) = 1/R_c, \quad (4.32)$$

where one assumes $\bar{M}_0 = -19.3$ mag, $\sigma_{M_0} = 2.0$ mag, $\sigma_{x_*} = 1$ and $\sigma_{c_*} = 1$. The priors on x_* and c_* are taken as Gaussian because this is the maximum-entropy prior on variables that can take positive and negative values, and for which one has an expectation for the mean and variance. In this case a mean of zero and a standard deviation of unity is appropriate. Since the widths R_x and R_c are non-negative scale parameters, we adopt the non-informative Jeffreys prior on them.

All the necessary integrals in Eq. 4.18 and Eqs. 4.22-4.24 are Gaussian, except those over R_x and R_c . Thus, March et al. (2011) integrate analytically to obtain a final expression for the likelihood in terms of an integral over only R_x and R_c ; these parameters are therefore added to the parameter vector ϕ , sampled from and marginalised out numerically to recover $\mathcal{L}_{\text{BHM}}(\phi)$ defined in Eq. 4.18.

One can see from Figure 4.5, that the BHM shows the same level of precision for parameter estimates as the standard χ^2 method, so both methods yield unbiased parameter constraints. For the BHM, however, one obtains two additional benefits: (i) the full probability distribution for σ_{int} ; and (ii) the ability to perform consistent Bayesian inference, including model selection. In Paper I, I compare the χ^2 -method and BHM in much more detail. I applied both of these methods to more realistic examples than the toy example used in this chapter and to real data (see Paper I and Section 6.1).

In spite of these advantages, one should also mention some shortcomings of BHM. First, a key difference between BHM and the standard χ^2 -method is that \mathcal{L}_{BHM} does not depend on M_0 , since this parameter is marginalised out analytically. Similarly, so too are the hidden variables M_i , which correspond to the “true” absolute magnitude of each SN. Consequently, one cannot calculate the residuals in Eq. 4.10 for each SN. This can make it difficult to compare the BHM with other methods, since visual inspection of the residuals often plays an important role. A further, and perhaps more critical, shortcoming of the BHM is the assumption that the hidden variables c_i and $x_{1,i}$ do not depend on redshift; this is a very crude approximation that is almost certainly not true. In the event that these quantities do evolve with redshift, one may show using simulations that the BHM can begin to produce biased parameter constraints, whereas the standard χ^2 -method is more robust to this effect, even though the formulation does not explicitly allow for this eventuality; this is illustrated in Figure 4.6.

4.6 Generalised Bayesian Likelihood

The above shortcomings of the BHM result from the assumption of simple (redshift-independent) Gaussian priors on the hidden variables and nuisance

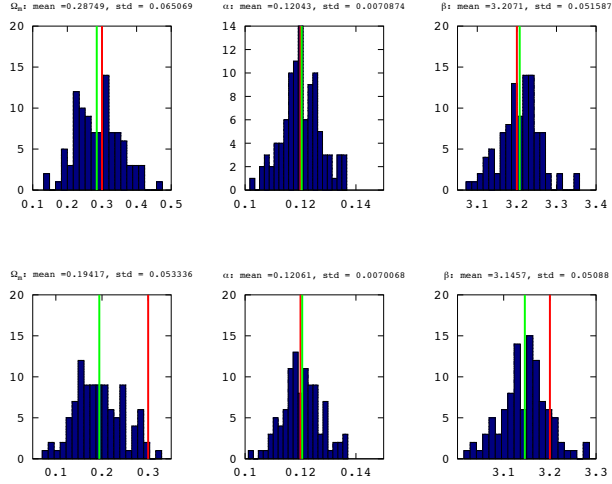


Figure 4.6: The same as Figure 4.5, but for SNe with $x_1(z > 0.5) = x_1(z < 0.5) + 1$, analysed using the χ^2 -method (top row) and the BHM (bottom row).

parameters, which is necessary in order to marginalise over them analytically. Consequently, it is of interest to retain the overall structure of the BHM, but to replace the analytical marginalisation with a numerical one. This results in a larger computational burden, but allows for the imposition of more realistic priors on the hidden variables, including redshift dependence, and provides access to best-fit values (indeed full marginal posterior distributions) of the hidden variables.

It therefore seems natural to improve upon the BHM as follows, to produce a Generalised Bayesian Likelihood.

1. Integrate Eq. 4.18 and Eqs. 4.22-4.24 numerically by sampling from the set of hidden parameters $x_{1,i}$, c_i , z_i , M_i ($i = 1, 2, \dots, N$) and nuisance hyper-parameters M_0 , x_* , R_x , c_* , R_c (in addition to the parameters of interest $\bar{\Phi}$), and numerically (as opposed to analytically) marginalising over them.
2. Allow for more realistic priors on the hidden and nuisance parameters than the simple separable Gaussian forms assumed in the BHM, in particular including the possibility of redshift dependence of c_i and $x_{1,i}$.

The resulting approach does, however, carry with it a substantially increased computational burden compared to the BHM, since the dimension of the parameter space to be sampled is increased by $4N + 5$, where N is the number of SNe being analysed. Even for existing SN data-sets, such as Union2 with over 600 SNe, this leads to a parameter space with over 2000 dimensions. To sample from a posterior distribution of this dimensionality and evaluate the evidence exceeds the current capabilities of the widely used Bayesian inference code MULTINEST. Therefore alternative methods are required. Provided the posterior distribution is relatively benign, i.e. smooth, unimodal and without very pronounced tails, then MCMC methods, such as Gibbs or Hamiltonian sampling, can produce reliable parameter estimates, and be combined with thermodynamic integration to evaluate the evidence. Another possibility is to use alternative forms of nested sampling, such as the DNest algorithm (Brewer, Pártay, & Csányi 2010), which is considerably less efficient than MultiNest up to around 50 dimensions, but is capable of producing posterior samples and evidence estimates in spaces with several thousand dimensions. I am currently investigating these various alternative sampling methods, and plan to present the Generalised Bayesian Likelihood and its application to real and simulated SN data in a forthcoming publication.

Chapter 5

Gravitational lensing of SNe

‘Light thinks it travels faster than anything but it is wrong. No matter how fast light travels, it finds the darkness has always got there first, and is waiting for it.’

Terry Pratchett

General relativity predicts that light rays are bent around massive bodies or, more generally, undergo deflections when they traverse a region in which the gravitational field is inhomogeneous. This effect is relevant to the study of SNe since the mass distribution along the line-of-sight to a SN will cause a gravitational lensing effect. The discussion in the previous chapter, and indeed in most papers on SN cosmology, ignores this effect. Nonetheless, such gravitational lensing can be used to constrain the form of the galaxy dark matter haloes along the lines-of-sight to the SNe, as I show in Paper II and Section 6.2. In this chapter I therefore give a brief description of some of the basic features of gravitational lensing.

5.1 Lens equation

Ray-tracing in curved spacetime, as illustrated in Figure 5.1, can be described by a lens equation,

$$\vec{\theta}_S = \vec{\theta}_1 - \frac{D_{LS}}{D_S} \alpha, \quad (5.1)$$

where $\vec{\theta}_S$ is the angle between source and the lens that would be observed in absence of lensing, $\vec{\theta}_1$ is the observed angle between image and lens, and α is the

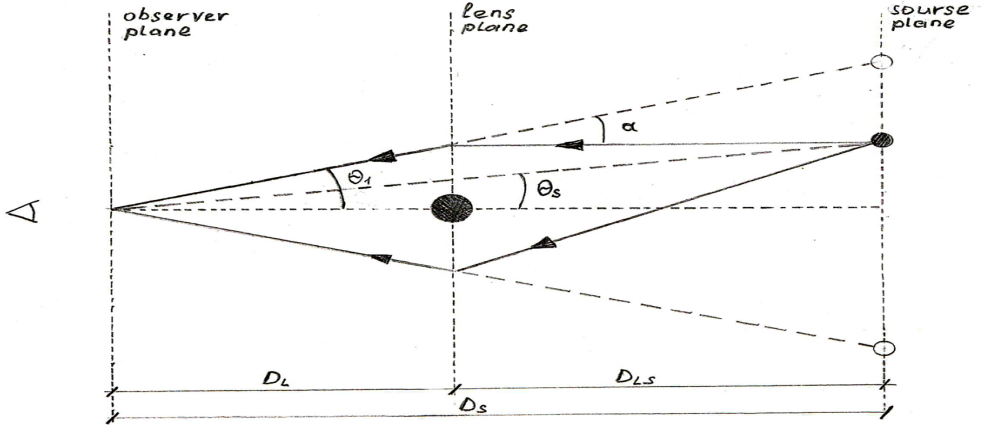


Figure 5.1: Gravitational lens geometry.

deflection angle; all the distances are angular-diameter distances D_A , since these are defined such that $D_A = \ell / \Delta\theta$, where ℓ is the proper transverse distance and $\Delta\theta$ is the angle it subtends at the observer. In our expanding Universe, for objects at redshift z_A and z_B , the angular-diameter distance is given by

$$D_{z_A z_B} = \frac{1}{(1+z_B)H_0} \int_{z_A}^{z_B} \frac{dz}{\sqrt{\Omega_{m,0}(1+z)^3 + \Omega_{\Lambda,0}}}, \quad (5.2)$$

where I have set $c = 1$.

In the case of a point mass lens, with mass M , Eq. 5.1 becomes

$$\theta_s = \theta_1 - \frac{D_{LS}}{D_S D_L} \frac{4GM}{\theta_1}. \quad (5.3)$$

In the very extreme case in which the source and lens are collinear, the source will be lensed into an Einstein ring and the angular separation is given by the Einstein angle:

$$\theta_E = \sqrt{\frac{4GM D_{LS}}{D_S D_L}}. \quad (5.4)$$

Thus for each lens one may define a critical surface mass density, above which one obtains an Einstein ring or multiple images; this is given by

$$\Sigma_c = \frac{1}{4\pi G} \frac{D_S D_L}{D_{LS}}, \quad (5.5)$$

Now, if one considers a more general lens than a point mass, for any surface density $\Sigma(\theta_1)$, which is obtained by projecting the matter distribution on to the

lens plane, one can introduce the dimensionless scaled surface mass density, or convergence $\kappa(\vec{\theta}_1)$, given by

$$\kappa(\vec{\theta}_1) = \frac{\Sigma(\vec{\theta}_1)}{\Sigma_c}. \quad (5.6)$$

In other words, the convergence describes the focussing by the lens of the light emitted by the source. This focussing causes the source to appear larger. According to Liouville's theorem (conservation of the phase-space density of the photons emitted by the source), the increase of size will lead to increase of brightness. At the same time, distortion by twisting of the light rays in the lens can occur. This will lead to shearing of the image shape.

To describe both phenomena one can introduce the lens map

$$A = \begin{pmatrix} 1 - \kappa - \gamma_1 & -\gamma_2 \\ -\gamma_2 & 1 - \kappa + \gamma_1 \end{pmatrix},$$

where $\gamma_1 = \gamma \cos(2\phi)$ and $\gamma_2 = \gamma \sin(2\phi)$, with γ being the ellipticity and ϕ is a position angle for an initially circular source that has been lensed into an ellipse. In terms of the convergence and shear one can define the important quantity known as the magnification:

$$\mu = \frac{1}{(1 - \kappa)^2 - \gamma^2}, \quad (5.7)$$

which corresponds to the ratio of the image area to the source area.

5.2 Types of gravitational lensing

The obvious case of interest is when the source is within the Einstein angle of the lens and multiple images, arcs, or even distinct parts of an Einstein ring appear; this is called strong gravitational lensing. Although predicted long before, the first multiple-image system was discovered by [Walsh et al. \(1979\)](#).

Observing multiple images of the same source, one can estimate the lens matter density distribution from simple Euclidean space calculations. One can also use the fact that some of the sources vary with time, so the multiple images could also vary with time. Time delays of the multiple images are another powerful mechanism which can be used to calculate the Hubble constant.

Strong lensing is often divided into subcategories, depending on the angular resolution of the images. Using the point source approximation in Eq. 5.4 we can get a feeling for the amount of the lensing in typical astronomical situations:

$$\begin{aligned}\theta_E &= 0.9 \sqrt{\left(\frac{M}{M_\odot}\right) \left(\frac{10 \text{ kpc}}{D}\right)} \text{ milliarcseconds} \\ &= 0.9 \sqrt{\left(\frac{M}{10^{11} M_\odot}\right) \left(\frac{\text{Gpc}}{D}\right)} \text{ arcseconds}\end{aligned}\quad (5.8)$$

The above estimates relate, respectively, to the two most commonly occurring situations: microlensing and macrolensing. Microlensing is interesting since lenses range from about the mass of a planet to the mass of a star. Microlensing is commonly used to: (i) constrain the nature of dark matter, for example in searches for MACHOs (massive compact halo objects); (ii) detect extrasolar planets; (iii) constrain the structure of the Milky Way disk, and do much more. Macrolensing, with separations of typically arcseconds, is the range where most of the collected images occur, so macrolensing is often a synonym for strong lensing itself.

Depending on the alignment of the lens and source, weak lensing could appear. Calling this lensing “weak” we should remember that it is not necessarily less important. Usually, weak lensing occurs when the lens is located outside the Einstein radius, and compared to strong gravitational lensing, results in small magnifications and small image distortions, which makes it often impossible to detect it without a priori knowledge of the source properties. While strongly lensed images often can tell us about the structure of the lens, weak gravitational lensing images allow us only to probe the statistical properties of the matter distribution on the line-of-sight. Nevertheless, weak lensing is one of the most common effects observed in the Universe. At some level, all objects that emit light and are observed at Earth are affected.

5.3 SNe through gravitational telescopes

Zwicky had already proposed by the 1930s to use galaxies as gravitational lenses. However, it was not until the late 1970s that the first gravitationally lensed objects were detected. From the very beginning, SNe have been taken into account in the calculation of the lensed images as being one of the background sources (Refsdal 1964). Since that time several applications of lensed SNe have been explored.

Unfortunately, no multiply imaged SN has yet been observed. Nevertheless, magnification/demagnification by large-scale structure along the line-of-sight can be used to estimate weak lensing effects.

This effect is a statistical “nuisance” in obtaining cosmological inferences from SNIa. There are two ways to correct for it: (i) assume some overall magnification distribution (e.g. [Holz & Linder 2005](#); [Martel & Premadi 2008](#)) or (ii) calculate convergence along each SN line-of-sight using simplified scaling relations applied to the nearby foreground galaxies observed (e.g. [Jönsson et al. 2008](#); [Jönsson et al. 2010b](#); [Kronborg et al. 2010](#); [Kostrzewa-Rutkowska, Wyrzykowski, & Jaroszyński 2013](#); [Smith et al. 2014](#)). The last method can also be used to estimate parameters of the objects on the line-of-sight, such as dark matter halo parameters, which I have done in Paper II and Section 6.2.

In recent wide-field surveys, a few SNe have been found that are detectably magnified. Among them are three gravitationally lensed SNe (SN CLO12Car, SN CLN12Did, and SN CLA11Tib) behind CLASH clusters ([Patel et al. 2014](#)). The reason for lensed SNe to be such rare events is that the SN has to be precisely aligned with a gravitational lens.

Chapter 6

Summary of my results

‘In God we trust. All others must bring data.’

W. Edwards Deming

My main research results are in the five papers included in this thesis, which describe different aspects of how observations of SNe can be used in astrophysics and cosmology. In particular, the papers focus on: the use of SNIa in constraining the background cosmological model describing our Universe; the use of gravitational lensing of distant SNIa by foreground cosmic structure to constrain the nature of dark matter haloes of galaxies; the determination from photometric lightcurves of whether or not a given SN is of type Ia, and hence can be used in cosmological inference; checking for consistency between different SN data-sets within large compilations. In this chapter, I will summarise the results from my papers, give an update on the already published results and describe findings that are yet to be published.

6.1 SNe and cosmology

In Chapter 4, I have already presented a general account of different methods for cosmological inference from SNIa data. In Paper I, I present a detailed comparison of the standard χ^2 -methodology and the recently proposed BHM applied to SNIa lightcurves fitted with the SALT2 technique. I described these two methods in Section 4.4 and 4.5 respectively. Through the analysis of realistically simulated SN data-sets, I obtain similar results in Paper I to those obtained from the toy example described in Chapter 4.

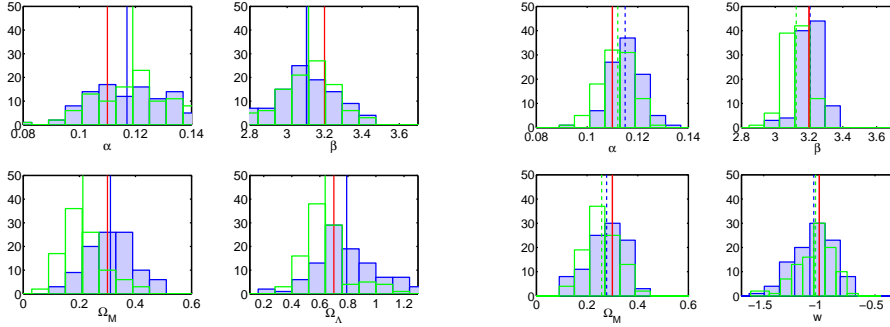


Figure 6.1: Left (right) panel: sampling distributions derived from a Λ CDM analysis of 100 simulated SNLS (‘cosmology’) data-sets. The histograms show the point estimates for the SNIa global parameters α, β and the cosmological parameters $\Omega_{m,0}, \Omega_{\Lambda,0}$, inferred using the BHM (filled blue histograms) and the chi-square method (empty green histogram). Blue and green vertical lines show the mean values of the point estimates, solid red vertical lines show the value of the true (i.e. model input) parameter used to simulate the data. From Paper I.

6.1.1 Biases in the χ^2 -method and BHM

In Paper I, I establish that small biases in the recovery of cosmological parameters occur for both the standard χ^2 -methodology and the BHM. These biases are not the same for each method, however, leading to discrepancies between their results, which are greatest when analysing just a single survey, such as SNLS; see the left panel in Figure 6.1. I find that the BHM offers a modest advantage over the χ^2 -method in that it produces slightly less biased estimates of the parameters; this is particularly true for $\Omega_{m,0}$. The biases on the $\Omega_{m,0}$ estimates produced by the two methods are in opposite directions, which results in approximately a 2σ discrepancy for any given realisation of SNLS-type data. Most interestingly, I find this to be the case for the real SNLS data-set. However, in simulations, one finds that increasing the redshift range of the data-set reduces the discrepancy between the methods; see the right panel of Figure 6.1. As more higher and lower redshift SNIa are added to the sample, the estimates of the cosmological parameters of interest from the two methods begin to converge. Nonetheless, this conclusion may be premature; although we generated state-of-the-art simulations, they contained no redshift dependence of the SN properties.

Data-set	Union2			S11		
	$\log(\mathcal{Z}_{H_{12}})$	$\log(\mathcal{Z}_{H_{22}})$	$\log(\mathcal{Z}_{H_{13}})$	$\log(\mathcal{Z}_{H_{12}})$	$\log(\mathcal{Z}_{H_{22}})$	$\log(\mathcal{Z}_{H_{13}})$
ESSENCE	9.21	10.18	8.57	—	—	—
HST	0.80	−0.16	0.23	−0.30	−0.63	−1.07
SDSS	−0.25	−0.77	−1.13	−0.33	−0.61	−1.27
SNLS	2.08	1.34	1.41	4.87	3.62	3.68
CfA	0.00	−0.20	−0.95	−0.01	−0.32	−1.02
Low- z	—	—	—	0.01	−0.30	−0.97

Table 6.1: log-evidence values for models $H_{n_\alpha n_\beta}$ (n_α and n_β being the number of redshift bins for stretch and colour parameter populations respectively) relative to the model H_{11} . Errors on these log-evidence values are all around 0.09.

6.1.2 BHM with redshift-dependent stretch and colour corrections

As mentioned in Chapter 4, it is possible for the stretch and colour parameter populations to evolve with redshift; indeed some studies have already tried to explore this possibility (Kessler et al. 2009; Conley et al. 2011). Kessler et al. (2009), in their Section 10.2.3, present evidence for the redshift evolution of the color parameter β for the SALT2 lightcurve fitting algorithm for different combinations of samples in the full data-set. This question has been revisited in Section 5.7 of Conley et al. (2011); they find that using later versions of SALT2 results just in marginal evidence for the evolution of the parameter β , but they do not discuss how this changes with different combinations of data-sets. I revisit this question by applying the BHM to the data from Union2 and Sullivan et al. (2011) (hereafter S11). I divide these SNe according to the telescope with which they have been observed; in particular I divide the SNe into the following subsets: ESSENCE, HST, SDSS, SNLS, CfA and a compilation of low- z SNIa measurements.

In order to check whether these data-sets have redshift evolution in the stretch and colour parameters, I modify the BHM to allow for this evolution by introducing multiple contiguous redshift bins for the stretch and colour parameter populations. SNe within different stretch (colour) redshift bins are allowed to have different values of α (β) and R_x (R_c). This is achieved by allowing the priors on α (β) and R_x (R_c) to be completely independent in different stretch (colour) redshift bins. The lower (upper) limits on first (last) redshift bin are set to z_{\min} (z_{\max}), where z_{\min} and z_{\max} are the minimum and maximum SN

redshifts in the catalogue. The other end points of redshift bins are set as free parameters which are estimated along with other BHM parameters. The number of stretch and colour redshift bins, represented by n_α and n_β , are estimated by Bayesian model selection, done by analysing models with different values of n_α and n_β , starting with $n_\alpha = n_\beta = 1$, and picking the model with the highest value for the Bayesian evidence. We denote these models by $H_{n_\alpha n_\beta}$.

The log-evidence values for models H_{12} , H_{22} and H_{13} , all with respect to the base model H_{11} , are given in Table 6.1. It is evident from this table that H_{12} ($n_\alpha = 1$, $n_\beta = 2$) is the preferred model for most data-sets. Even when H_{12} is not the most preferred model, preference for other models over it is not very strong. Thus, in agreement with the previous studies mentioned above, we see that our Bayesian model selection approach also provides evidence for some evolution with redshift of the β parameter. This is an interesting finding in its own right, but also has important consequences for using the standard BHM, which assumes no redshift dependence for any of the parameters. Clearly, this assumption is broken by the real data, and so one must take care in interpreting results obtained using the “vanilla” BHM. Although the modification to the BHM introduced above has its uses, a more statistically-principled approach to extending the BHM is to allow the priors on the colour and stretch parameters to depend on redshift. This generalised Bayesian likelihood method is discussed in Section 4.6.

6.2 SNe and cosmic structure

In Paper II, I present a Bayesian statistical methodology for constraining the properties of dark matter haloes of foreground galaxies that intersect the lines-of-sight towards SNIa. This builds on the BHM used in Paper I.

In this approach, the parameters of interest are those describing the dark matter haloes assumed to exist around the known galaxies along the lines-of-sight to the SNIa. My method yields an effective likelihood function, which gives the probability of obtaining the observed SNIa data (i.e. the parameter values obtained in SALT2 lightcurve fits) as a function of these parameters. Once appropriate priors have been placed on the parameters, the full posterior distribution is explored using MULTINEST to obtain parameter constraints and also calculate the Bayesian evidence for use in model comparison.

I investigate two different models for the density profile $\rho(\mathbf{r})$ of the dark matter halo: the truncated singular isothermal sphere (tSIS) and the Navarro–Frenk–White (NFW) profile (Navarro, Frenk, & White 1997), both of which are widely used models in astronomy. My results for the SIS profile are presented in

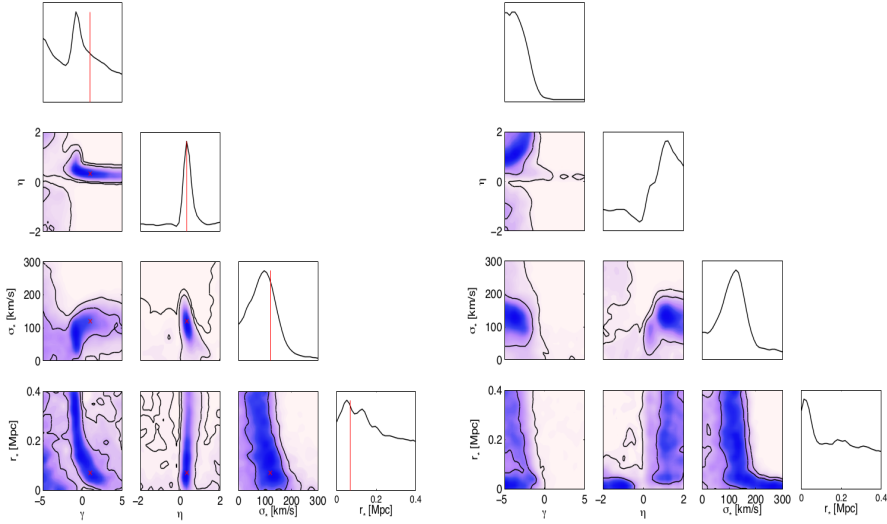


Figure 6.2: Left (right) panel: 1D and 2D marginalised posteriors distributions for the parameters of the tSIS halo model, derived from the analysis of 500 simulated SNIa generated from a tSIS model (real SNLS data). From Paper II.

Paper II. The NFW results were also included in the first version of Paper II, but were subsequently removed during the refereeing process, since it was necessary to add significant further discussion of the methodology, which resulted in the paper becoming too long. I summarise below the main finding for both the SIS and NFW profiles; note that the full version of the original paper is still online as the 1st arXiv version of Paper II.

6.2.1 SIS model

The SIS model has a radial density profile given by

$$\rho(r) = \frac{\sigma^2}{2\pi G} \frac{1}{r^2}, \quad (6.1)$$

which is a function of just one single free parameter, namely the one-dimensional velocity dispersion σ of its constituent particles. A disadvantage of the SIS profile is that the total mass diverges. Consequently, I use a modified version that depends on a second free parameter r_t , which defines the radius at which the SIS profile is truncated. For finite r_t , the total mass does not diverge.

It is straightforward to show that for an object described by a tSIS profile, the surface density is

$$\Sigma(\xi) = \begin{cases} \frac{\sigma^2}{\pi G \xi} \arctan \sqrt{r_t^2/\xi^2 - 1} & \text{if } \xi \leq r_t \\ 0 & \text{if } \xi > r_t. \end{cases} \quad (6.2)$$

By substituting this expression into Eq. 5.6, one obtains the corresponding convergence $\kappa_{\text{gal}}(\xi)$ produced by a galaxy dark matter halo of this form.

An important complication that arises is the potential relationship between the velocity dispersion and the galaxy luminosity. To allow for this possibility and to determine the form of the relationship, I assume the scaling relations:

$$\sigma = \sigma_* \left(\frac{L}{L_*} \right)^\eta, \quad (6.3)$$

$$r_t = r_* \left(\frac{\sigma}{\sigma_*} \right)^\gamma = r_* \left(\frac{L}{L_*} \right)^{\eta\gamma}, \quad (6.4)$$

Thus, for the tSIS halo model, we wish to constrain the four parameters $\mathbf{h} = \{\gamma, \eta, \sigma_*, r_*\}$.

To evaluate my methodology, I first apply it to simulated SNIa data-sets. To this end, I generate and analyse multiple sets of simulations, each the same size as the real SNLS data-set. My main finding was that there is a wide variation in the significance at which one may detect a gravitational lensing signal. This results from the strong dependency of the gravitational lensing signal on whether the data sample contains some SNIa that are strongly magnified. The number of such SNIa in the sample has a marked effect on the derived log-evidence $\Delta \log \mathcal{Z}$ relative to a model assuming no lensing, which I find ranges from about -1.5 to 4.5 , with a median value of -0.6 . The parameter constraints derived from this median catalogue are very broad; indeed the constraints are similar to those obtained from a simulation containing no lensing signal. Nonetheless, as shown in the left panel of Figure 6.2, if one increases the number of SNe in the data-set up to 500, the constraints become much tighter and one is able to set limits on the parameters of the dark matter haloes. Indeed, these constraints contain the true values input to the simulations. Thus, provided the sample of SNe is sufficiently large, my method is able to detect the gravitational lensing signal and recover the correct halo parameters.

When applied to real SNLS data (consisting of 162 SNIa), the parameters constraints are those shown in the right panel of Figure 6.2. On performing a Bayesian model comparison, I find that the model for a lensing signal produced by tSIS haloes is only just preferred by 0.2 log-evidence units relative to the

no lensing model, which is similar to the uncertainty in the evaluated evidence. Consequently, there is no support for choosing either the lensing or no lensing models. This marginal detection is contrary to previous studies, although these earlier works did not perform Bayesian model selection, but instead focussed on goodness-of-fit statistics at the best-fit point in parameter space. One can begin to reconcile these findings by noting that the parameter constraints for the tSIS halo model (see the right panel of Figure 6.2) do appear somewhat tighter than those obtained for simulations of 162 SNIa without the inclusion of a lensing signal. This does suggest a borderline detection of a lensing signal in the real SNLS data.

6.2.2 NFW model

The NFW profile has a radial density distribution given by

$$\rho(r) = \frac{\delta_c \rho_c}{(r/r_s)(1 + r/r_s)^2}, \quad (6.5)$$

where $\rho_c = 3H^2(z)/8\pi G$ and $H(z)$ are the critical density and Hubble parameter, respectively, at the redshift, z , of the halo. The scale radius $r_s = r_{200}/c$ is a characteristic radius for the halo, where r_{200} (the virial radius) is the radius at which the mass density of the halo drops to $200\rho_c$, the dimensionless number c is the concentration parameter, and

$$\delta_c = \frac{200}{3} \frac{c^3}{\ln(1+c) - c(1+c)^{-1}} \quad (6.6)$$

is a characteristic overdensity. The profile therefore depends on two free parameters: the virial radius r_{200} and the concentration parameter c .

The mass contained within the virial radius r_{200} is

$$M_{200} \equiv M(r \leq r_{200}) = \frac{800\pi}{3} \rho_c r_{200}^3 = \frac{800\pi}{3} \frac{\rho_m}{\Omega_m} r_{200}^3, \quad (6.7)$$

where ρ_m is the mean matter density of the universe and Ω_m is the matter density parameter, both evaluated at the redshift z of the halo.

To evaluate the gravitational lensing effect of an NFW halo, one must calculate its surface density, which is given by (Bartelmann 1996)

$$\Sigma(\xi) = \begin{cases} \frac{2r_s \delta_c \rho_c}{(x^2-1)} \left[1 - \frac{2}{\sqrt{1-x^2}} \operatorname{arctanh} \sqrt{\frac{1-x}{1+x}} \right] & (x < 1) \\ \frac{2r_s \delta_c \rho_c}{3} & (x = 1) \\ \frac{2r_s \delta_c \rho_c}{(x^2-1)} \left[1 - \frac{2}{\sqrt{x^2-1}} \arctan \sqrt{\frac{x-1}{x+1}} \right] & (x > 1) \end{cases} \quad (6.8)$$

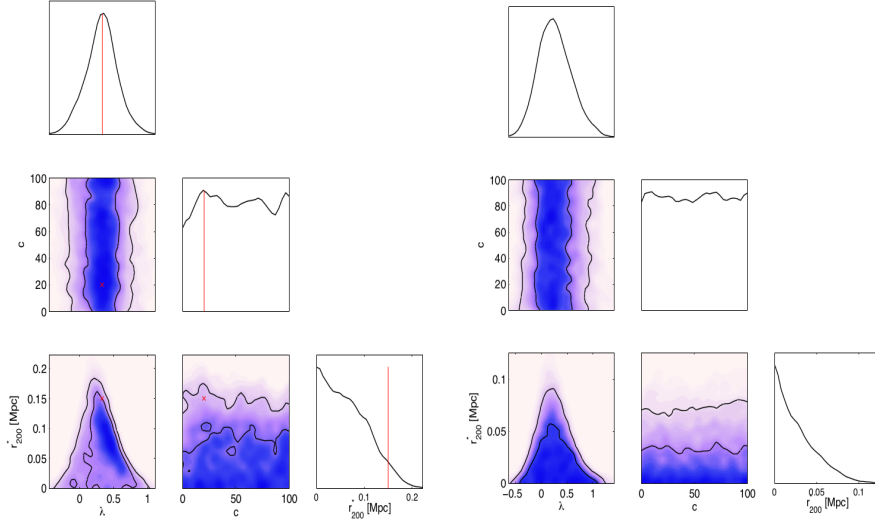


Figure 6.3: 1D and 2D marginalised posteriors distributions for the parameters $\mathbf{h} = \{\lambda, c, r_{200}^*\}$ of the NFW halo model, derived from the analysis of 162 simulated SNIa data generated assuming no lensing (right) and a NFW halo model (left). In the left-hand panel, true parameters are indicated by vertical lines and crosses in 1D and 2D plots, respectively.

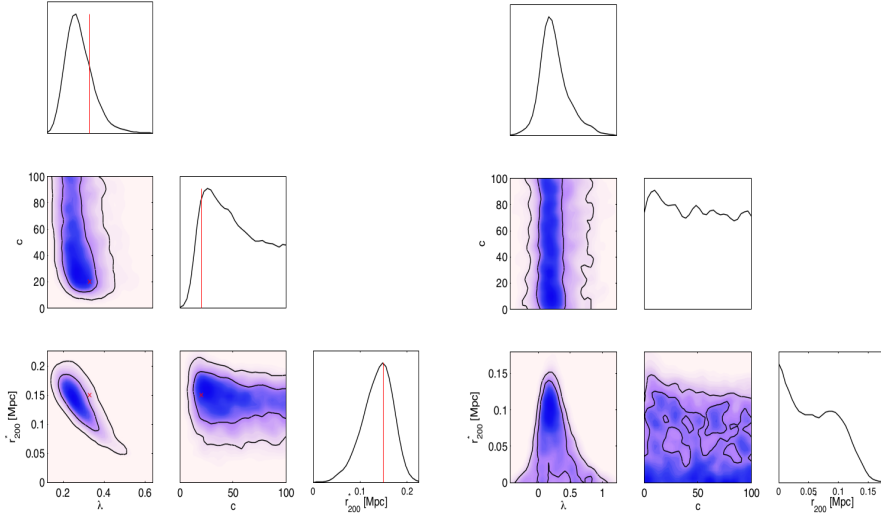


Figure 6.4: As in Figure 6.2, but for $\mathbf{h} = \{\lambda, c, r_{200}^*\}$ of the NFW model.

Analysis model	Simulation model		
	No lensing	tSIS	NFW
No lensing	0.0	0.0	0.0
tSIS	-1.8	-1.1	-1.3
NFW	-3.1	-2.6	-2.3

Table 6.2: $\Delta \log \mathcal{Z}$ (log-evidence value relative to the null evidence) for the analysis of simulated data with 162 SNIa, with errors of 0.2.

where $x = \xi/r_s$ is a dimensionless projected radial distance in the lens plane. The resulting convergence $\kappa_{\text{gal}}(\xi)$ due to a NFW halo is then obtained by substituting $\Sigma(\xi)$ into Eq. 5.6.

A complication arises similar to that encountered for the tSIS profile, namely that there is potentially a relationship between the virial radius of a NFW halo and the luminosity of the galaxy it surrounds. To allow for and investigate this possibility, I therefore adopt the scaling law

$$r_{200} = r_{200}^* \left(\frac{L}{L_*} \right)^\lambda. \quad (6.9)$$

In this case, one thus seeks to constrain the three parameters $\mathbf{h} = \{\lambda, c, r_{200}^*\}$.

I first apply my method to simulated data-sets of the same size (162 SNIa) as the real SNLS data, as was done for tSIS model. Figure 6.3 shows that one cannot obtain any real constraints on the NFW halo parameters, since the marginalised posteriors look very similar to those obtained from simulations containing no lensing signal. Increasing the number of SNe in the simulations to 500, I find that my method does produce constraints on the halo parameters that are consistent with the input values used in the simulations; this is illustrated in the left panel of Figure 6.4. As shown in the right panel, however, the analysis of the real SNLS data yields no useful constraints on the halo parameters.

6.2.3 Model selection between different dark matter halo models

To understand better the marginal detection (at best) of any lensing signal in the real SNLS data, I now perform a systematic Bayesian model comparison using my simulated data-sets. I begin by considering simulations of the same size (each containing 162 SNIa) as the real SNLS data. Table 6.2 lists the Bayesian log-evidence for each analysis model, relative in each case to the null

Analysis model	Simulation model		
	No lensing	tSIS	NFW
No lensing	0.0	0.0	0.0
tSIS	-1.7	4.5*	6.9
NFW	-3.1	3.6	7.2*

Table 6.3: $\Delta \log \mathcal{Z}$ (log-evidence value relative to the null evidence) for the analysis of simulated data with 500 SNIa, with errors of 0.2. Asterisks denote the cases for which the corresponding halo parameter constraints are plotted in the left panels of Figs. 6.2 and 6.4, respectively.

Model	$\Delta \log \mathcal{Z}$
tSIS	0.2*
NFW	-2.5*

Table 6.4: $\Delta \log \mathcal{Z}$ (log-evidence value relative to the null evidence for no lensing signal) for the analysis of the real SNIa data, with errors of 0.2. Asterisks denote the cases for which the corresponding halo parameters constraints are plotted in the right panels of Figs 6.2 and 6.4, respectively.

(no-lensing) model. In each case, the no lensing model is preferred. This concurs with my findings for the real SNLS data, and suggests that one cannot detect a lensing signal with data of this quantity and quality, let alone distinguish between different halo models.

To determine the nature of the data required to obtain a robust detection of lensing, I analyse simulations each containing 500 SNIa. The results are given in Table 6.3. For simulations containing no lensing signal, the method correctly identifies this as the preferred model. More importantly, however, my method also prefers the models with lensing (at high significance) for simulations that do contain a lensing signal. This demonstrates that the method performs correctly. Moreover, the correct halo model is also picked out, although the selection between halo models is not robust as the log-evidence differences are quite small.

Finally, Table 6.4 shows the results using real data. As mentioned above, for the tSIS halo model, there is a very slight preference for a lensing signal, but only by 0.2 log-evidence units, which is the level of the uncertainty in the calculation of the evidence. For the NFW halo model, however, the presence of a lensing signal is strongly disfavoured by -2.5 log-evidence units relative to

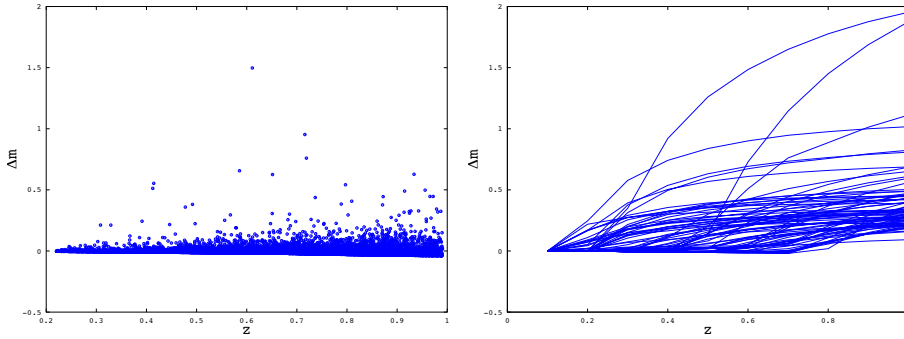


Figure 6.5: Left: magnification of 10^4 simulated SNIa. Right: magnification for the 75 lines-of-sight that exhibit the strongest lensing effect. From Paper II.

the no lensing model.

6.2.4 Foreground galaxies catalogue

In all the analyses described in this section, I have used the *true* galaxies from the SNLS catalogue. To understand my results further, it is of interest to examine the magnification along a large number of lines-of-sight through these galaxies.

In Figure 6.5 (right panel), I plot the magnification factor for each of 10^4 simulated SNIa. From the plot, one can see that the background correction results in most of the SNIa being demagnified. Nonetheless, there are a small number of SNIa that have very large magnifications. This suggests that one should expect a large variation in the strength of the lensing signal when analysing SNIa catalogues containing relatively few events, such as the SNLS data-set. The important criterion is whether the SNIa catalogue contains one or more SNIa that are very strongly magnified. As one observes more SNIa, one would expect the variation between randomly constructed catalogues to diminish, and a more stable and robust detection of lensing to be possible. This agrees with my results given above.

Another important observation is that, for strongly magnified SNIa, there is no clear correlation between the size of the magnification and redshift. This suggests the counter-intuitive conclusion that observing high-redshift SNIa may not confer any advantage in attempting to detect a lensing signal. I examine this issue further by plotting in Figure 6.5 (right panel) the magnification as a function of redshift along the 75 lines-of-sight that exhibit the highest magnification. One first notices that the magnification of the three most highly lensed

lines-of-sight continues to increase markedly up to $z = 1$. Nonetheless, for the remaining lines-of-sight, the magnification does not typically increase much beyond $z \sim 0.5$. Again this suggests that, at least along these lines-of-sight, there is little advantage in observing a very high-redshift SNIa in terms of detecting a lensing signal.

One must be careful in drawing such conclusions, however, because I am using the true galaxy catalogue from SNLS. This real catalogue will inevitably suffer from selection effects that result in high-redshift galaxies being under-represented. This is expected to give the above effects. One may investigate this issue further by performing the same analysis for galaxy catalogues constructed taken from some large numerical simulation, and this would be an interesting topic for future research. Moreover, forthcoming surveys such as DES and Euclid will enable us to take a significant step forward, since they will provide not only SNIa data, but also very good measurements of foreground galaxies.

6.3 SNe photometric classification

In Section 3.2, I started a discussion about methods that can perform photometric classification of SNe into Ia and non-Ia types. Since such methods are becoming increasingly necessary for the analysis of large SNIa data-sets, I also worked on developing fully automated methods that can perform this task in a quick, automated and robust manner. In Paper III, I present a new method for performing automated photometric classifications of SNe into Ia and non-Ia types. This method adopts an extremely naive approach to the question and I do not use any prior information about SNe physics. Thus in Paper V, I use a HNN to include information about SN models. Both of these methods take a two-stage approach. First, the SN lightcurves are fitted to an analytic parameterised function in order to standardise the number of variables associated with each SN. The resulting fitted parameters, together with a few further quantities associated with the fit, are then used as the input feature vector to a classification NN and a hierarchy of classification NNs whose output is the probability that the SN is of a particular type.

6.3.1 First step: Lightcurve fitting

The form of the fitted function is given by

$$f(t) = A [1 + B(t - t_1)^2] \frac{e^{-(t-t_0)/T_{\text{fall}}}}{1 + e^{-(t-t_0)/T_{\text{rise}}}}, \quad (6.10)$$

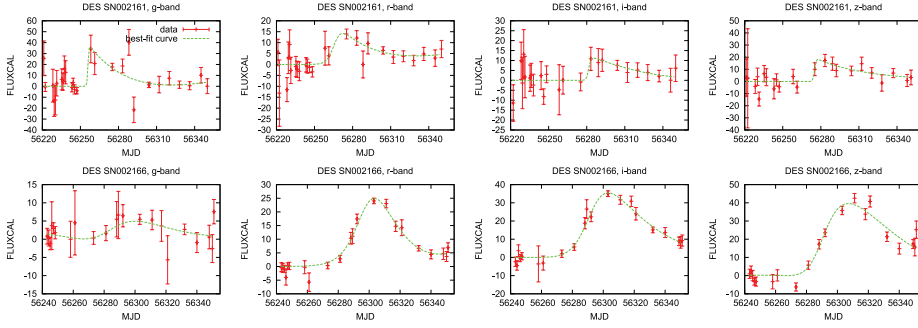


Figure 6.6: Simulated lightcurve measurements and associated uncertainties (red points) in the g , r , i and z filters for a Type-Ia (top row) and non-Ia (bottom row) SN, together with the best-fit function (green line). From Paper III.

where, for each SN, $t = 0$ corresponds to the time of the earliest measurement in the r -band lightcurve. Figure 6.6 shows the best-fitting functional form in four wavebands for a typical Ia and non-Ia SN.

For each fitted lightcurve, I construct a feature vector that contains the mean values of the one-dimensional marginalised posteriors of each parameter in the fitting formula of Eq. 6.10, $\hat{\Theta} = \{\hat{A}, \hat{B}, \hat{t}_1, \hat{t}_0, \hat{T}_{\text{rise}}, \hat{T}_{\text{fall}}\}$ and their standard deviations $\sigma = \{\sigma_A, \sigma_B, \sigma_{t_1}, \sigma_{t_0}, \sigma_{T_{\text{rise}}}, \sigma_{T_{\text{fall}}}\}$. I also append to the feature vector the number of flux measurements n in the lightcurve, the maximum-likelihood value of the fit and the Bayesian evidence of the model. This feature vector then provides a standardised input for the training of the NN.

6.3.2 Second step: NN classification

In Section 2.3, I described the 3-layer feed-forward NNs that I use in my work. In particular, I use the SkyNet package.

In the application to SN classification, it is important to assess the quality of the network output classes by constructing some statistical measures. The most appropriate quantities are the completeness ϵ_{Ia} (fraction of all SNIa that have been correctly classified; also often called the efficiency), purity τ_{Ia} (fraction of all Type Ia candidates that have been classified correctly) and figure of merit \mathcal{F}_{Ia}

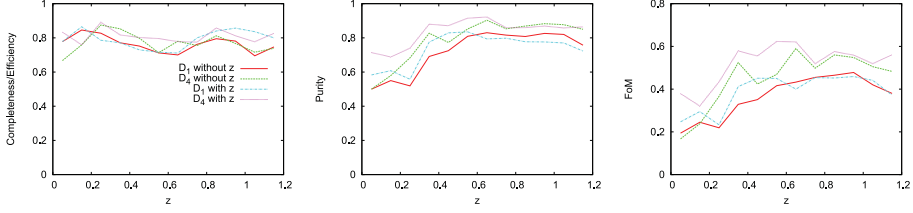


Figure 6.7: Completeness, purity and figure of merit for SNIa classification as a function of redshift (z) from applying trained networks with a threshold probability (p_{th}) of 0.5; “with z ” and “without z ” indicates that redshift information was/was not used in network training. Samples \mathcal{D}_1 and \mathcal{D}_4 use 10 and 40 per cent of the data, respectively, for training. From Paper III.

for SNIa. These are defined as follows:

$$\epsilon_{\text{Ia}} = \frac{N_{\text{Ia}}^{\text{true}}}{N_{\text{Ia}}^{\text{total}}}, \quad (6.11)$$

$$\eta_{\text{Ia}} = \frac{N_{\text{Ia}}^{\text{true}}}{N_{\text{Ia}}^{\text{true}} + N_{\text{Ia}}^{\text{false}}}, \quad (6.12)$$

$$\mathcal{F}_{\text{Ia}} = \frac{1}{N_{\text{Ia}}^{\text{total}}} \frac{(N_{\text{Ia}}^{\text{true}})^2}{N_{\text{Ia}}^{\text{true}} + W N_{\text{Ia}}^{\text{false}}}, \quad (6.13)$$

where $N_{\text{Ia}}^{\text{total}}$ is the total number of SNIa in the sample, $N_{\text{Ia}}^{\text{true}}$ is the number of SNe correctly predicted to be of Type Ia, $N_{\text{Ia}}^{\text{false}}$ is the number of SNe incorrectly predicted to be of Type Ia and W is a penalty factor which controls the relative penalty for false positives over false negatives.

6.3.3 SuperNova Photometric Classification Challenge (SNPCC)

I started my work on developing methods for photometric classification of SNe by applying it to the updated simulated data-set released following the SNPCC (Kessler et al. 2010a,b). I did not apply any cuts to the original data, so my data-set contained low signal-to-noise SNe and very poorly-sampled lightcurves, sometimes containing very few measured fluxes that are not necessarily measured on both sides of peak brightness.

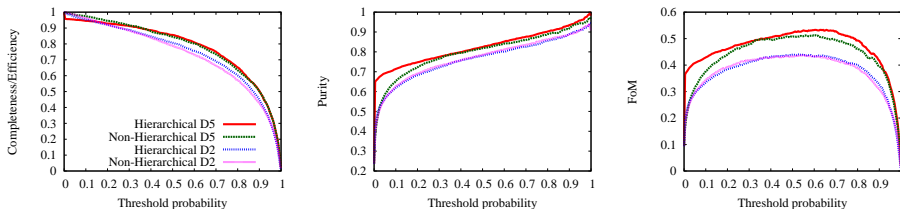


Figure 6.8: Completeness, purity and FoM as a function of threshold probability p_{th} from applying trained networks to get Ia/non-Ia classification probabilities on the testing data-set from NN (Paper III) and HNN. No redshift information was used in network training. Samples \mathcal{D}_2 and \mathcal{D}_5 use 20 and 50 per cent of the data, respectively, for training. From Paper V

NN

In Paper III, I found that applying a regular classification network, I obtain very robust classification results, namely a completeness of 0.78 (0.82), purity of 0.77 (0.82), and SNPCC figure-of-merit of 0.41 (0.50) when I use 10 (40) per cent of the data for training and assume a canonical threshold output probability $p_{th} = 0.5$. I pick my training set randomly and do not use any redshift information. A modest 5–10 per cent improvement in these results is achieved by also including the SN host-galaxy redshift and its uncertainty as inputs to the classification network, see Figure 6.7. The quality of the classification does not depend strongly on the SN redshift.

HNN

In Paper V, I further develop the method presented in Paper III by introducing a HNN, which accommodates the structure shown on Figure 3.2. From Figure 6.8 we see that HNN performs better than the method in Paper III as more training data becomes available. Even with a small amount of data, however, HNN still performs well. These positive preliminary results motivates further study, in particular the investigation of the importance of the training sample: is it percentage or total number of SNe used for training that makes the largest difference? Also I want to test this method on a more realistic sample, for example when measurements for some filters are missing completely.

6.4 Testing consistency

In Section 3.3.3, I described the benefits of using a joint analysis of SNe from different telescopes/surveys, having SNe both at low and high redshift. A large collection of SNe over a wide range of redshifts results in tighter constraints on cosmological parameters. This comes at a price, however, since one must first check that the individual SN surveys produce results that are mutually consistent. If this is not the case, any results derived from their combination may be misleading. Such checks for mutual consistency are rarely performed. In Sections 2.1.1 and 2.1.2 I discussed Bayesian methods to perform such a test. In this Section, I apply this method to SN data.

6.4.1 Consistency test based on χ^2 -method

In Paper IV, I test the mutual consistency of different SN surveys within JLA (Betoule et al. 2014) and Union2 compilations. The same way as in Section 6.1.2 I separate each compilation into subsets according to the telescope/survey with which they have been observed. Since the χ^2 -method uses a non-normalised likelihood one replaces $\Pr(\mathbf{D}|\Theta, H)$ by the “likelihood” $\mathcal{L}(\Theta, \sigma_{\text{int}})$ discussed in Section 4.4. In this case, however, one can no longer interpret the terms in Eq. 2.5 directly as probabilities. Consequently, the value of the \mathcal{R} cannot be compared with the normal Jeffreys’ scale. One still expects, however, that for data-sets that are mutually consistent the \mathcal{R} -value will be higher than for inconsistent ones March et al. (2011b). Consequently, one may still use the \mathcal{R} -value, but as a one-sided test statistic in the frequentist sense, which must be calibrated using simulations.

The distribution of \mathcal{R} under the null hypothesis H_0 is constructed from simulations in which the individual surveys are mutually consistent. The \mathcal{R} value obtained by analysing the real data can then be compared with this distribution in the standard manner. In particular, we calculate the p -value as:

$$p = \frac{N(\mathcal{R}_s < \mathcal{R}_r)}{N_{\text{tot}}}, \quad (6.14)$$

where \mathcal{R}_s and \mathcal{R}_r are the \mathcal{R} values obtained by analysing simulated and real data-sets respectively, $N(\mathcal{R}_s < \mathcal{R}_r)$ is the number of simulations with \mathcal{R} values less than that obtained by analysing the real data and N_{tot} is the total number of simulations.

My key finding is that the multipliers α and β of the stretch and colour corrections, respectively, are significantly different for the Union2 catalogue (see the left panel of Figure 6.9). By contrast, the JLA catalogue shows no such

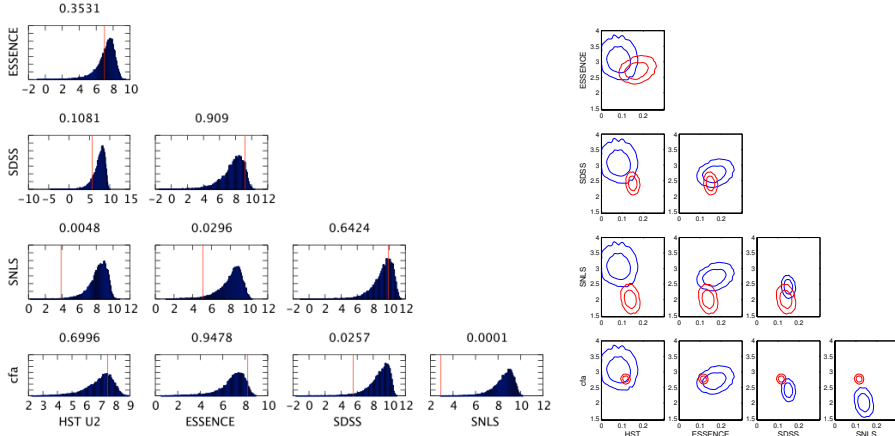


Figure 6.9: Left panel: Results of the consistency test applied to survey pairs in the Union2 compilation. The blue histograms show the distribution of \mathcal{R} -values obtained from 10⁴ consistent simulations of each pair, and the red vertical line indicates the \mathcal{R} -value obtained from the real data. The corresponding one-sided p -value is given above each panel. Right panel: Two-dimensional marginalised constraints on the parameters (α, β) obtained from the individual constituent surveys contained in the Union2 catalogue. The red (blue) contours denote the 68 and 95 per cent confidence regions for the survey in that row (column). From Paper IV.

inconsistency. Interestingly, both catalogues show no inconsistency in the constraints derived on cosmological parameters. Nonetheless, the inconsistency discovered for the Union2 catalogue means that one must be careful interpreting the results obtained from a joint analysis of it. The results of the consistency test for the Union2 compilation are shown in the left panel of Figure 6.9, together with the corresponding p -values.

6.4.2 Consistency test based on BHM

In contrast to the χ^2 -method, using BHM allows one to use the \mathcal{R} -test directly, as described in Section 2.1.1. Since I use here the same data as in Section 6.1.2, I will use BHM with two bins for colour parameters as the default hereafter.

In Tables 6.5 and 6.6, I summarise the results for pairwise consistency checks of the S11 and Union2 data-sets respectively. I should recall here that positive (negative) values of $\log(\mathcal{R})$ give evidence in favour of consistency (inconsistency) between data-sets with the level of consistency (inconsistency) inter-

	HST	SDSS	SNLS	CfA
SDSS	3.97	—	—	—
SNLS	1.50	8.33	—	—
Low- z	3.24	8.28	-3.50	—
CfA	3.46	8.09	1.54	6.13

Table 6.5: $\log(\mathcal{R})$ -values for pairwise consistency tests of data-sets in the S11 catalogue. Errors on these $\log(\mathcal{R})$ -values are all around 0.18.

	ESSENCE	HST	SDSS	CfA
HST	10.62	—	—	—
SDSS	-16.42	6.19	—	—
SNLS	4.84	8.01	13.47	—
CfA	7.47	6.21	-12.17	-0.42

Table 6.6: $\log(\mathcal{R})$ -values for pairwise consistency checks of data-sets in the Union2 catalogue. Errors on these $\log(\mathcal{R})$ -values are all around 0.18.

puted according to Jeffreys' scale given in Table 2.1. From Tables 6.5 and 6.6, we see that, as for the consistency check based on the χ^2 -method, some data-sets are inconsistent within the Union2 catalogue.

The level of inconsistency between different SN data-sets in the Union2 catalogue again means that one should be careful interpreting the results from joint analysis performed using this compilation. One should note, however, that the inconsistent pairings derived in the BHM analyses are different to those found using the χ^2 -method. This is not surprising, as the two methods are very differently affected by redshift dependence of SN properties, as discussed in Chapter 4, and the BHM method used here is explicitly allowing for such an effect. Nonetheless, in both the BHM and χ^2 -method, the inconsistencies found are related to the β parameter associated with the colour correction.

6.4.3 Hyper-parameters

Here I present results from analysing the SN data-sets from Section 6.1.2 using the hyper-parameter approach described in Section 2.1.2.

In my work I will introduce the hyper-parameters γ_i , one for each data-set, by modifying the covariance matrix \hat{C}_i of data-set D_i to become $\hat{C}_i/\sqrt{\gamma_i}$. This

Data-set	Union2
ESSENCE	0.49 ± 0.11
HST	0.65 ± 0.18
SDSS	0.78 ± 0.22
SNLS	0.46 ± 0.09
CfA	0.17 ± 0.06

Table 6.7: Estimated values of the hyper-parameters γ_i for the Union2 catalogue.

explicitly allows for the possibility that the quoted measurement uncertainties are over or under-estimated, but may be considered more generally as a weighting of each data-set. As discussed in [Hobson, Bridle, & Lahav \(2002\)](#), the prior distribution on the hyper-parameters γ_i is exponential with expectation value unity. This follows because one expects *a priori* the quoted measurement uncertainties from each data-set to be neither over- nor under-estimated. With this constraint, and the requirement that the weights are non-negative, the correct prior distribution according to the maximum-entropy principle is the exponential prior (see e.g. [Hobson, Bridle, & Lahav 2002](#)).

First I perform model selection between the two hypotheses.

H_0 : The combined data-set can be described without hyper-parameters γ_i , i.e. the data-sets are all consistent with each other and measurement uncertainties are neither over- nor under-estimated.

H_1 : The combined data-set requires the hyper-parameters γ_i , in order to deal with inconsistencies between data-sets and/or inaccuracies in the measurement uncertainties.

For the S11 and Union2 catalogues, $\log(\mathcal{Z}_{H_0}/\mathcal{Z}_{H_1})$ is found to be 2.30 ± 0.17 and -8.54 ± 0.18 , respectively. These values point towards inconsistency between different data-sets in the Union2 catalogue which is in perfect agreement with our findings in the last section using the \mathcal{R} -test. The S11 catalogues did not show any inconsistency between different data-sets according to the \mathcal{R} -test, which is reinforced by their preference for a model without hyper-parameters γ_i .

Estimated values of hyper-parameters γ_i are given in Table 6.7. In the absence of any inconsistencies or measurement inaccuracies, one should expect $\gamma_i \sim 1$, therefore any deviation from unity provides evidence in favour of some unaccounted systematics in the data-set. It can be seen from Table 6.7 that in the

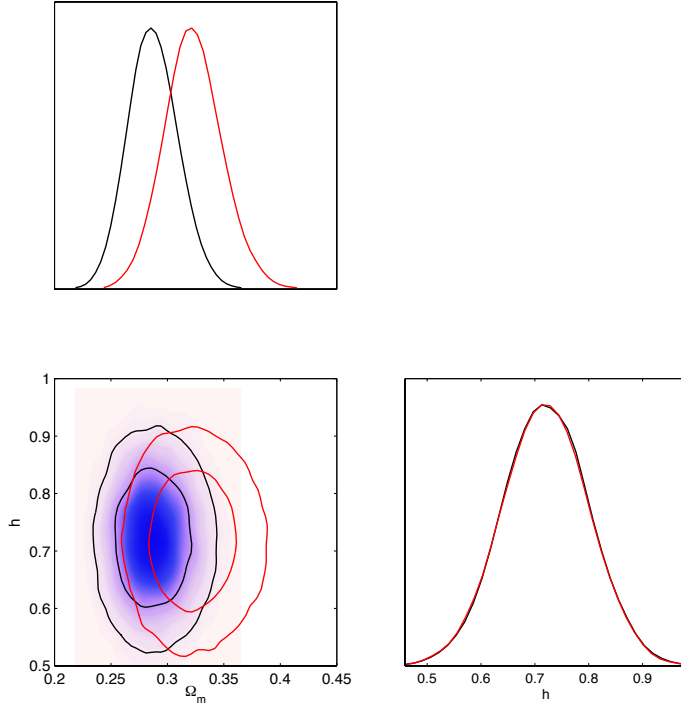


Figure 6.10: 1D and 2D marginalised posterior distributions for the matter density $\Omega_{m,0}$ and Hubble parameter h when the Union2 catalogue is analysed with (red) and without (black) hyper-parameters γ_i .

Union2 catalogue, ESSENCE, SNLS and CfA, all have γ_i more than 3σ away from unity. In order to show the effect of these systematics on cosmological parameter inferences, we plot the marginalised posterior distributions for the matter density $\Omega_{m,0}$ and Hubble parameter h when the Union2 catalogue is analysed with and without hyper-parameters γ_i . Introduction of hyper-parameters results in a 15% increase in the estimated value of $\Omega_{m,0}$, as shown in Figure 6.10. Hence it is important to include these effects.

Chapter 7

Outlook

‘Let the past look after itself, and
let the present move forwards into
the future’

Douglas Adams

7.1 Future problems for SN astronomy

SN data helped observational cosmology to make a great step forward over the last two decades. The discovery of the accelerated expansion of the Universe undoubtedly is one of the most important breakthroughs over the past 20 years. Unfortunately, the nature of it still remains unknown. Nevertheless, future SN surveys certainly will help our understanding of this great mystery of 21st century physics. Already today, SN data are good enough to perform model selection between different cosmological scenarios. Future SN surveys will address all these problems, not only by increasing the number of observed SNe, thereby improving the statistical errors, but also by focussing on systematics. The problems discussed in Chapter 4 regarding rigorous inference methods will be more important than ever, which will inevitably lead to the development of more robust methods for cosmological parameter inference.

Another big question in SN studies is the nature of the SN explosion itself. Standard models for SNIa explosions, such as a carbon-oxygen white dwarf burning and the merger of two white dwarfs, are increasingly questioned for their universality. On the other hand, the nature of core-collapse SNe is an even bigger puzzle, resulting in our inability even to write a parametric function for the non-Ia lightcurves. The solution to this problem does not relate to cosmology

per se, but will inevitably have a huge influence on cosmological parameter inference. Knowing an explosion mechanisms will play a crucial role in a better standardisation of SNe.

Observing SNe in multiple filters proved to be key to their standardisation. Future surveys will increase the number of filters, which will not only help to better standardise events, but will open a window for spectroscopy-free SNe cosmology. Having measurements of lightcurves in multiple filters in the future will allow us to make classification based only on photometry. Already, some photometric classification methods seems to be very competitive. Improving these methods will be one of the main objectives for future photometric surveys. For example, as was mentioned before, knowing the exact explosion mechanism for different types of SNe will be a great advantage, since having a parametric function for all SN types will allow us to make model selection between different SN types, as opposed to performing the comparison using template methods.

In discussing spectroscopy-free cosmology, however, it is important not to belittle the importance of high-quality spectroscopic data. Such data is a cornerstone of SN cosmology. New experiments, such as iPTF and ZTF, will have on-line spectroscopic follow-up for all detected SNe. Having high-resolution spectroscopic data at the epochs as close as possible to the explosion will give us invaluable information to study the explosion mechanisms. Having a large data-set of spectroscopically-classified SNe is also of a great importance for developing the photometric classification algorithms mentioned above.

Another interesting path for SN cosmology is to try to standardise non-Ia SNe. As I discussed in Section 3.5, SNII-P have proved to be viable candidates for making cosmological inferences. With a better understanding of “standard” SN types and with “modern” SNe, such as SLSNe, or types yet to be discovered, we can try in the future to make a cosmological inference based on more than one type, or even using all of them.

One might summarise the current status of SN cosmology by saying that, although it blossomed in 1998, the fruits are only now becoming ripe.

7.2 My interest for the coming years

The Bayesian methods I developed during my PhD years are ideally suited for investigating the problems discussed in the previous section. Since the statistical methods I am working with are very general in nature, I would like to broaden my research interests into other neighbouring topics, such as the CMB and large-scale structures, as well as more areas in gravitational lensing. In particular, I

wish to apply my experience with Bayesian parameter estimation and model selection to these areas. Building on my work with SNIa, one area of considerable interest would be to apply my Bayesian methods for testing the consistency of data-sets to a wider range of cosmological probes. There are already hints from Planck and SNIa data that the two data-sets disagree on the value of the Hubble parameter. This could be a real cosmological effect, or the result of undiagnosed systematics. Also, as cosmological data-sets improve, it will become possible to distinguish the standard concordance cosmology from alternative models at greater significance. As the signal-to-noise ratio of data improves, one (somewhat ironically) has to be *more* careful in performing statistical analyses, as systematic effects begin to emerge from the noise. My Bayesian methods are again ideally suited to investigate such problems.

As the final words of my “The supernova cosmology cookbook”, I would like to quote my favorite physicist, Lev Davidovich Landau: “Cosmologists are often in error, but never in doubt”.

Финальными словами моей “Поваренной книги о сверхновых в космологии: Байесовские численные рецепты” я хочу процитировать моего любимого физика Льва Давидовича Ландау “Астрономы часто ошибаются, но никогда не сомневаются”.

Appendix A

Princes cake

A.1 Ingredients

Cake:

- 4 eggs
- 2 dl sugar
- 1 dl flour
- 1 dl potato flour
- 2 teaspoons baking powder

Filling:

- 4 sheets of gelatine
- 2 dl vanilla sauce
- 2 teaspoons vanilla sugar
- 3 dl whipping cream

Garnish:

- 300 g marzipan
- green and red food dye
- icing sugar

A.2 What to do

Cake:

1. Preheat the oven to 175 C.
2. Grease and dust a round shape, about 2.5 liters.
3. Beat eggs and sugar until fluffy. Mix the two flours and baking powder and fold into the batter and mix well. Pour into mold. Bake in the lower part of the oven for about 40 minutes. Turn the cake and let it cool.

Filling:

1. Add the gelatine leaves to cold water. Boil the mix of the vanilla sauce according to package directions. Remove the gelatine leaves and squeeze them well. Place them in the hot vanilla sauce.
2. Whip the cream until thick. Stir in the vanilla sauce when the cream starts to thicken. Let the cream become almost solid.

Cut the cake into 3 layers (for 1 cake). The top should be slightly less than 1 inch thick. Flatten the layers with filling between. Save a bit of it. Let the filling be slightly higher in the middle so the cake will be puffy when the uppermost thin layer is put on. Spread the rest of the cream on top and around the edge.

Garnish:

1. Colour about 70% of the marzipan green and the remaining marzipan red (it will become more pink than red).
2. Roll the green marzipan into a round, thin, smooth sheet. It should be enough to cover the entire cake with an even thickness.
3. Cut out a circle sector with an area of about 30% of the area of the full sheet.
4. Roll the pink marzipan to a sheet big enough to cover the piece which was cut out from the green.
5. Cut out a circle segment with the same size as that which was removed before.
6. Cover the cake with the the green and pink marzipan pieces.
7. Sift icing sugar on top.

As done in many Swedish bakeries, put on top a pretty pink marzipan rose. The best is to find a rose with the mass of approximately 5% of the total marzipan mass composing your cosmology cake.

A.3 When to eat

Princess cake is perfect for any occasion, but best (in the author's opinion) with a cup of Swedish filtered coffee on a cold winter day which lasts for four months.

References

- Ade P. A. R., et al., 2014, PhRvL, 112, 241101
- Albrecht A., et al., 2006, astro, arXiv:astro-ph/0609591
- Amanullah R., et al., 2010, ApJ, 716, 712
- Astier P., et al., 2005, astro, arXiv:astro-ph/0510447
- Astier P., Guy J., Regnault N., Pain R., Aubourg E., Balam D., Basa S., Carlberg R. G., Fabbro S., 2006, A&A, 447, 31
- Astier P., 2012, arXiv, arXiv:1211.2590
- The ATLAS Collaboration: G. Aad, et al., 2008, arXiv, arXiv:0901.0512
- Baade W., Zwicky F., 1934, Proceedings of the National Academy of Science, 20, 254
- Bailey S., et al., 2009, A&A, 500, L17
- Bartelmann M., 1996, A&A, 313, 697
- Bessell M. S., 1990, PASP, 102, 1181
- Betoule M., et al., 2014, ArXiv e-prints
- BICEP2 Collaboration, et al., 2014, arXiv, arXiv:1403.4302
- Blondin S., Prieto J. L., Patat F., Challis P., Hicken M., Kirshner R. P., Matheson T., Modjaz M., 2009, ApJ, 693, 207
- Branch D., 1992, ApJ, 392, 35
- Brewer B. J., Pártay L. B., Csányi G., 2010, ascl.soft, 10029
- Burns C. R., et al., 2011, AJ, 141, 19
- Conley A., et al., 2006, astro, arXiv:astro-ph/0607363
- Conley A., et al., 2008, ApJ, 681, 482
- Conley A., et al., 2011, ApJS, 192, 1
- Contreras C., et al., 2009, AAS, 214, #427.04
- Copin Y., et al., 2009, EAS, 36, 11
- Cox R. T., 1946, AmJPh, 14, 1
- D'Agostini G., 1995, ArXiv High Energy Physics - Phenomenology e-prints
- D'Agostini G., 2005, physics., arXiv:physics/0511182
- D'Andrea C. B., et al., 2010, ApJ, 708, 661

- de Zeeuw P. T., et al., 2000, *INGN*, 2, 11
- Diemand J., Kuhlen M., Madau P., 2007, *ApJ*, 657, 262
- Diemand J., Kuhlen M., Madau P., Zemp M., Moore B., Potter D., Stadel J., 2008, *Nature*, 454, 735
- Falck B. L., Riess A. G., Hlozek R., 2010, *ApJ*, 723, 398
- Feroz F., Hobson M. P., 2008, *MNRAS*, 384, 449
- Feroz F., Allanach B. C., Hobson M., Abdus Salam S. S., Trotta R., Weber A. M., 2008, *JHEP*, 10, 64
- Feroz F., Hobson M. P., Bridges M., 2009, *MNRAS*, 398, 1601
- Feroz F., Hobson M. P., Cameron E., Pettitt A. N., 2013, *arXiv*, arXiv:1306.2144
- Foley R. J., et al., 2009, *AJ*, 138, 376
- Foley R. J., Kasen D., 2011, *ApJ*, 729, 55
- Fukugita M., Ichikawa T., Gunn J. E., Doi M., Shimasaku K., Schneider D. P., 1996, *AJ*, 111, 1748
- Gal-Yam A., 2012, *Sci*, 337, 927
- Germany L. M., Reiss D. J., Schmidt B. P., Stubbs C. W., Suntzeff N. B., 2004, *A&A*, 415, 863
- Goldhaber G., et al., 2001, *astro*, arXiv:astro-ph/0104382
- Gong Y., Cooray A., Chen X., 2010, *ApJ*, 709, 1420
- Graff P., Feroz F., Hobson M. P., Lasenby A., 2012, *MNRAS*, 421, 169
- Graff P., Feroz F., Hobson M. P., Lasenby A. N., 2013, *AAS*, 221, #431.01
- Graff P., Feroz F., Hobson M. P., Lasenby A., 2014, *MNRAS*, 441, 1741
- Gull S., 1989, *Maximum Entropy and Bayesian Methods*, 511
- Gunn J. E., Siegmund W. A., Mannery E. J., 2006, *astro*, arXiv:astro-ph/0602326
- Guy J., Astier P., Nobili S., Regnault N., Pain R., 2005, *A&A*, 443, 781
- Guy J., et al., 2007, *A&A*, 466, 11
- Guy J., Sullivan M., Conley A., Regnault N., Astier P., Balland C., Basa S., Carlberg R. G., Fouchez D., Hardin D., Hook I. M., Howell D. A., Pain R., 2010, *aap*, 523, A7
- Hamuy M., Phillips M. M., Maza J., Suntzeff N. B., Schommer R. A., Aviles R., 1995, *AJ*, 109, 1
- Hamuy M., Phillips M. M., Suntzeff N. B., Schommer R. A., Maza J., Avilés R., 1996, *astro*, arXiv:astro-ph/9609062
- Hansen L., Jorgensen H. E., Norgaard-Nielsen H. U., 1987, *Msngr*, 47, 46
- Hayden B. T., et al., 2010, *ApJ*, 712, 350
- Hicken M., et al., 2009, *ApJ*, 700, 331
- Hillebrandt W., Niemeyer J. C., 2000, *astro*, arXiv:astro-ph/0006305
- Hobson M. P., Bridle S. L., Lahav O., 2002, *MNRAS*, 335, 377

- Hodapp K.-W., et al., 1996, *NewA*, 1, 177
- Hoeflich P., Khokhlov A., 1996, *astro*, arXiv:astro-ph/9602025
- Holtzman J. A., et al., 2008, *AJ*, 136, 2306
- Holz D. E., Linder E. V., 2005, *ApJ*, 631, 678
- Hornik K., Stinchcombe M., White H., 1990, *Neural Networks*, 3, 359
- Howell D. A., et al., 2005, *ApJ*, 634, 1190
- Howell D. A., et al., 2006, *Natur*, 443, 308
- Hoyle F., Fowler W. A., 1960, *ApJ*, 132, 565
- Iben I., Jr., Tutukov A. V., 1984, *ApJS*, 54, 335
- Ishida E. E. O., de Souza R. S., 2012, *ArXiv e-prints*
- Jha S., et al., 2006, *AJ*, 131, 527
- Jha S., Riess A. G., Kirshner R. P., 2007, *ApJ*, 659, 122
- Johnson B. D., Crotts A. P. S., 2006, *AJ*, 132, 756
- Jönsson J., Dahlén T., Goobar A., Mörtzell E., Riess A., 2007, *JCAP*, 6, 2
- Jönsson J., Kronborg T., Mörtzell E., Sollerman J., 2008, *A&A*, 487, 467
- Jönsson J., Dahlén T., Hook I., Goobar A., Mörtzell E., 2010a, *MNRAS*, 402, 526
- Jönsson J., Sullivan M., Hook I., Basa S., Carlberg R., Conley A., Fouchez D., Howell D. A., Perrett K., Pritchett C., 2010b, *MNRAS*, 405, 535
- Kessler R., et al., 2009, *ApJS*, 185, 32
- Kessler R., et al., 2010, *PASP*, 122, 1415
- Kessler R., Conley A., Jha S., Kuhlmann S., 2010, *arXiv*, arXiv:1001.5210
- Kim A. G., et al., 2013, *ApJ*, 766, 84
- Knop R. A., et al., 2003, *astro*, arXiv:astro-ph/0309368
- Kostrzewa-Rutkowska Z., Wyrzykowski Ł., Jaroszyński M., 2013, *MNRAS*, 429, 2392
- Kowalski M., et al., 2008, *ApJ*, 686, 749
- Kronborg T., et al., 2010, *A&A*, 514, A44
- Kunz M., Bassett B. A., Hlozek R. A., 2007, *Phys.Rev.D*, 75, 103508
- Kuznetsova N. V., Connolly B. M., 2007, *ApJ*, 659, 530
- LHC Higgs Cross Section Working Group, et al., 2011, *arXiv*, arXiv:1101.0593
- Li W. D., et al., 1999, *astro*, arXiv:astro-ph/9912336
- Mackay D. J. C., 2003, *Information Theory, Inference and Learning Algorithms*
- March M. C., Trotta R., Berkes P., Starkman G. D., Vaudrevange P. M., 2011, *MNRAS*, 418, 2308
- March M. C., Trotta R., Amendola L., Huterer D., 2011, *MNRAS*, 415, 143
- Martel H., Premadi P., 2008, *ApJ*, 673, 657
- Massey R., et al., 2007, *Nature*, 445, 286
- Miknaitis G., et al., 2007, *astro*, arXiv:astro-ph/0701043

- Minkowski R., 1941, *PASP*, 53, 224
- Minkowski R., 1964, *ARA&A*, 2, 247
- Mosher J., et al., 2014, *arXiv*, arXiv:1401.4065
- Navarro J. F., Frenk C. S., White S. D. M., 1996, *ApJ*, 462, 563
- Navarro J. F., Frenk C. S., White S. D. M., 1997, *ApJ*, 490, 493
- Newling J., Varughese M., Bassett B., Campbell H., Hlozek R., Kunz M., Lampeitl H., Martin B., Nichol R., Parkinson D., Smith M., 2011, *MNRAS*, 414, 1987
- Nomoto K., 1982, *ApJ*, 253, 798
- Nomoto K., Iwamoto K., Kishimoto N., 1997, *Sci*, 276, 137
- Norgaard-Nielsen H. U., Hansen L., Jorgensen H. E., Aragon Salamanca A., Ellis R. S., 1989, *Natur*, 339, 523
- Nugent P., Kim A., Perlmutter S., 2002, *PASP*, 114, 803
- Ó Ruanaidh J., Fitzgerald W., 1996, *Numerical Bayesian Methods Applied to Signal Processing*. Springer Verlag:New York
- Patel B., et al., 2014, *ApJ*, 786, 9
- Perlmutter S., et al., 1997, *ApJ*, 483, 565
- Perlmutter S., et al., 1999, *ApJ*, 517, 565
- Phillips, M. M. 1993, *ApJ*, 413, L105
- Phillips M. M., Lira P., Suntzeff N. B., Schommer R. A., Hamuy M., Maza J., 1999, *AJ*, 118, 1766
- Planck Collaboration, et al., 2013, *arXiv*, arXiv:1303.5076
- Poznanski D., Gal-Yam A., Maoz D., Filippenko A. V., Leonard D. C., Matheson T., 2002, *PASP*, 114, 833
- Poznanski D., Maoz D., Gal-Yam A., 2007, *AJ*, 134, 1285
- Prieto J. L., Rest A., Suntzeff N. B., 2006, *astro*, arXiv:astro-ph/0603407
- Refsdal S., 1964, *MNRAS*, 128, 307
- Rest A., et al., 2013, *arXiv*, arXiv:1310.3828
- Richards J. W., Homrighausen D., Freeman P. E., Schafer C. M., Poznanski D., 2012, *MNRAS*, 419, 1121
- Riess A. G., Press W. H., Kirshner R. P., 1996, *ApJ*, 473, 88
- Riess A. G., et al., 1998, *AJ*, 116, 1009
- Riess A. G., et al., 1999, *AJ*, 117, 707
- Riess A. G., et al., 2004, *ApJ*, 607, 665
- Riess A. G., et al., 2006, *astro*, arXiv:astro-ph/0611572
- Rodney S. A., Tonry J. L., 2009, *ApJ*, 707, 1064
- Sako M., et al., 2008, *AJ*, 135, 348
- Sako M., Bassett B., Connolly B., Dilday B., Cambell H., Frieman J. A., Gladney L., Kessler R., Lampeitl H., Marriner J., Miquel R., Nichol R. C., Schnei-

- der D. P., Smith M., Sollerman J., 2011, *ApJ*, 738, 162
- Scolnic D., et al., 2013, *arXiv*, arXiv:1310.3824
- Skilling J., 2004, in Fischer R., Preuss R., Toussaint U. V., eds, *American Institute of Physics Conference Series Vol. 119, Nested Sampling*. pp 1211–1232
- Smith M., et al., 2014, *ApJ*, 780, 24
- Springel V., White S. D. M., Jenkins A., Frenk C. S., Yoshida N., Gao L., Navarro J., Thacker R., Croton D., Helly J., Peacock J. A., Cole S., Thomas P., Couchman H., Evrard A., Colberg J., Pearce F., 2005, *Nature*, 435, 629
- Springel V., Frenk C. S., White S. D. M., 2006, *Natur*, 440, 1137
- Springel V., Wang J., Vogelsberger M., Ludlow A., Jenkins A., Helmi A., Navarro J. F., Frenk C. S., White S. D. M., 2008, *MNRAS*, 391, 1685
- Stritzinger M., Leibundgut B., 2004, *astro*, arXiv:astro-ph/0410686
- Sullivan M., et al., 2006, *AJ*, 131, 960
- Sullivan M., et al., 2011, *ApJ*, 737, 102
- Suzuki N., et al., 2012, *ApJ*, 746, 85
- Thielemann F.-K., Brachwitz F., Höflich P., Martinez-Pinedo G., Nomoto K., 2004, *NewAR*, 48, 605
- Thomas R., et al., 2009, *AAS*, 41, #489.02
- Tonry J. L., et al., 2003, *astro*, arXiv:astro-ph/0305008
- Tutukov A. V., Yungelson L. R., 1981, *NInfo*, 49, 3
- Tyson J. A., Kochanski G. P., dell’Antonio I. P., 1998, *ApJ*, 498, L107
- Walsh D., Carswell R. F., Weymann R. J., 1979, *Nature*, 279, 381
- Wang L., Goldhaber G., Aldering G., Perlmutter S., 2003, *astro*, arXiv:astro-ph/0302341
- Wang B., Han Z., 2012, *NewAR*, 56, 122
- Webbink R. F., 1984, *ApJ*, 277, 355
- Whelan J., Iben I., Jr., 1973, *ApJ*, 186, 1007
- Zwicky F., 1940, *Reviews of Modern Physics*, 12, 66